OPTICAL COMMUNICATIONS FOR TRANSPORT AIRCRAFT

ROBERT STENGEL
Department of Mechanical and Aerospace Engineering
Princeton University

THE PROBLEM

- Increasing demand for radio-frequency bands from an enlarging pool of users (aircraft, ground and sea vehicles, fleet operators, traffic control centers, commercial radio and television)
- Desirability of providing high-bandwidth, dedicated communications to and from every aircraft in the National Airspace System
- Need to support communications, navigation, and surveillance for a growing number of aircraft
- Improved meteorological observations by use of probe aircraft

THE SOLUTION

- Optical signal transmission support very high data rates
- Optical transmission of signals between aircraft, orbiting satellites, and ground stations, where unobstructed line-of-sight is available
- Conventional radio transmission of signals between aircraft and ground stations, where optical line-of-sight is unavailable
- Radio priority given to aircraft in weather

AEROSPACE OPTICAL COMMUNICATION

Data communications between aircraft and ground stations could be supported with direct and relayed signals. Aircraft at altitude typically would have unobstructed line of sight to an overhead spacecraft and frequently could communicate with other aircraft at similar altitude. Fiber-optic links on the ground complete the data path for air-ground links obscured by clouds through unobscured air-satellite-ground links.

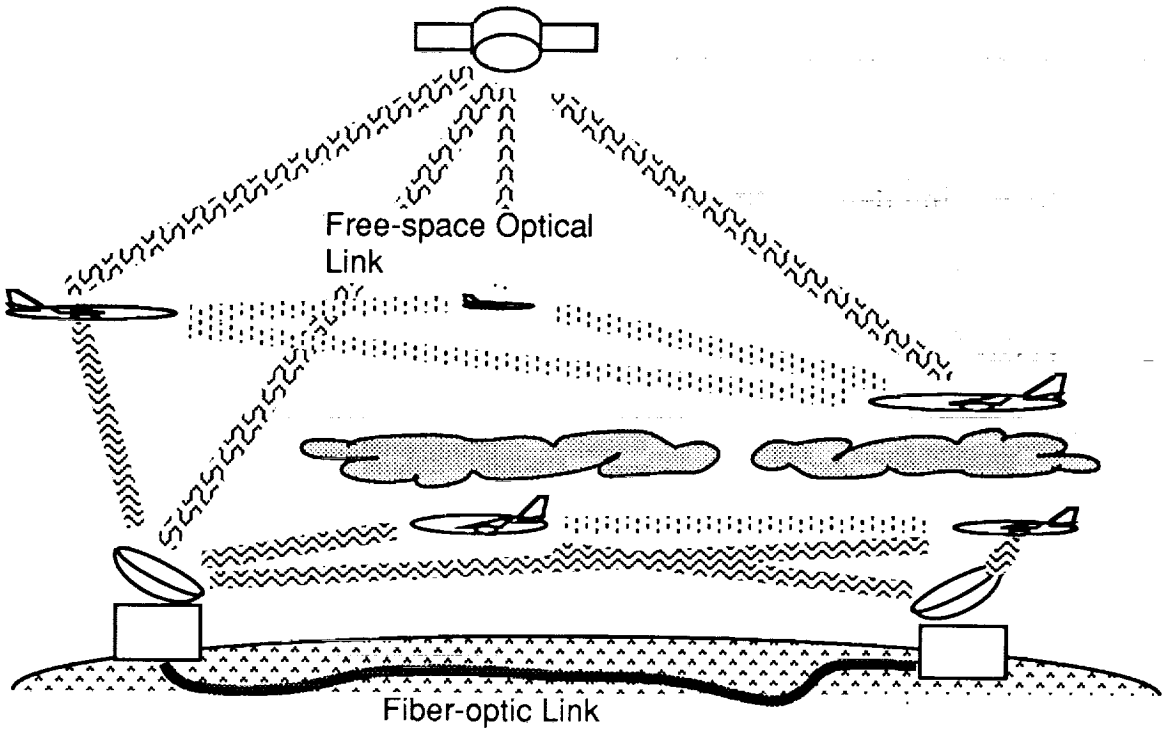

- Opportunistic Optical Transmission
- Distributed Network containing Free-Space and Fiber-Optic Links
- Radio Transmission where Optical Link is Unavailable

Typical Cloud Cover Patterns Across the United States

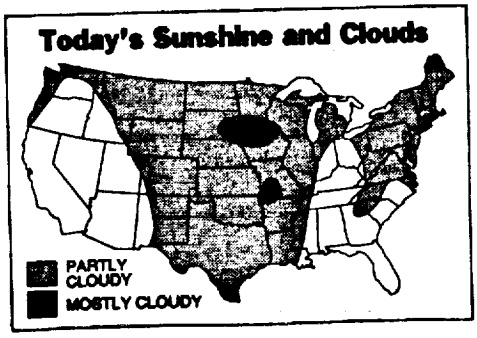

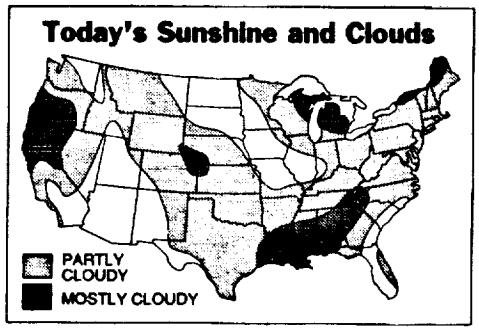

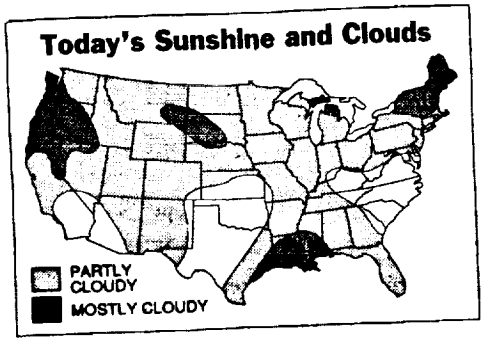

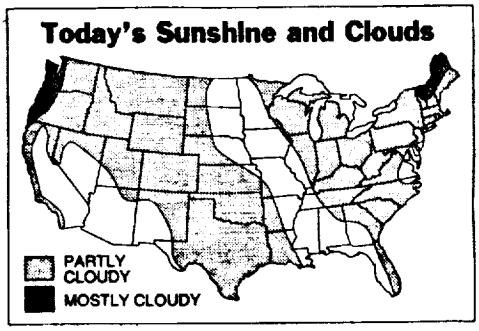

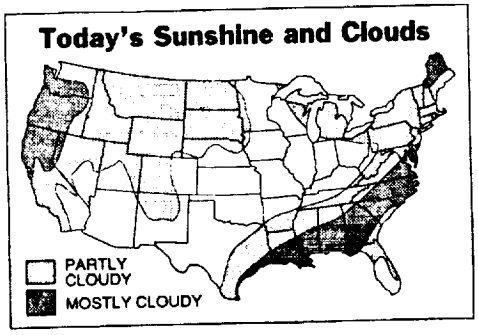

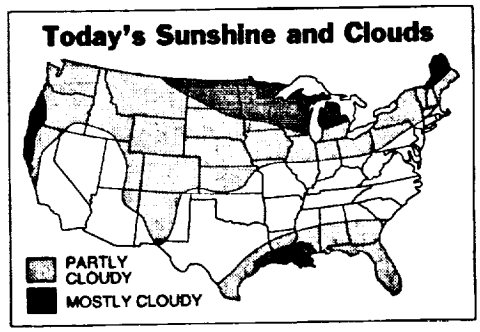

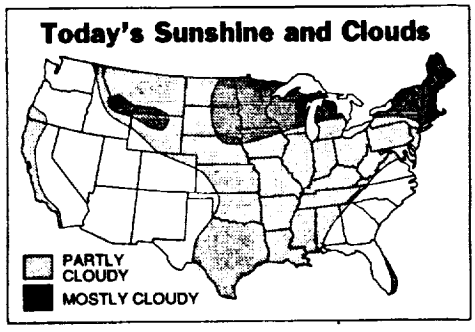

EVERY AIRCRAFT A WEATHER PROBE AND AIRBORNE SURVEILLANCE SYSTEM

Increased data bandwidth allows greatly expanded transfer of information about weather conditions and individual aircraft. Observational data from aircraft is integrated into a real-time four-dimensional weather map in ground-based computers. This information, in turn, becomes available to all aircraft in the system.

- DOWNLINK
  Own position and velocity vectors
  Own air temperature, pressure, and humidity
  Own wind velocity vector
  Own light intensity
  Own turbulence intensity
  Signal strengths from electrical activity and beacons
  Airborne hazard status monitoring and alerts
  Desired alternate flight plans

- UPLINK
  Air temperature, pressure, and humidity fields
  Wind and turbulence fields
  Cloud cover
  Traffic alerts
  Ground/satellite-based hazard status monitoring and alerts
  Arbitrated alternate flight plans

RESEARCH ISSUES

Numerous technical, operational, and institutional issues must be resolved before the suitability of optical communications for aircraft can be fully assessed. Many of these are topics for basic and applied research.

- Optical signal generation, transmission, and detection
- Coherence, filtering, power, multiplexing, and coding
- Coupling between optics and electronics
- Communication coverage modeling
- Telescope field of view, pointing, acquisition, and tracking
- Free-space/fiber-optic networking and data-relay protocols
- Architectures for CNS and ATM
- Interfaces with related systems
- Integration within an Intelligent Aircraft/Airspace System

Robustness of Solutions to a Benchmark Control Problem

Robert F. Stengel* and Christopher I. Marrison†
Princeton University, Princeton, New Jersey 08544

The robustness of 10 solutions to a benchmark control design problem presented at the 1990 American Control Conference has been evaluated. The 10 controllers have second- to eighth-order transfer functions and have been designed using several different methods, including H_∞ optimization, loop-transfer recovery, imaginary-axis shifting, constrained optimization, structured covariance, game theory, and the internal model principle. Stochastic robustness analysis quantifies the controllers' stability and performance robustness with structured uncertainties in up to six system parameters. The analysis provides insights into system response that are not readily derived from other robustness criteria and provides a common ground for judging controllers produced by alternative methods. One important conclusion is that gain and phase margins are not reliable indicators of the probability of instability. Furthermore, parameter variations actually may improve the likelihood of achieving selected performance metrics, as demonstrated by results for the probability of settling-time exceedance.

Introduction

CONTROL systems should be designed to maintain satisfactory stability and performance characteristics not only at nominal operating points but over a range of parameters that encompasses system uncertainty. These systems should be robust, but there is a limit. Unbounded robustness is no more attractive than inadequate robustness, because nominal performance and insensitivity to parameter variations tend to produce conflicting design requirements. Hence, the degree of robustness that must be furnished for satisfactory operation is related to the system variations that are most likely to occur.

Measures of robustness should be easily understood and should be directly connected to control design objectives. They should be consistent with what is known about the structure and parameters of the plant's dynamic model. These goals are best served when robustness is expressed in terms of the likelihood that commonly accepted properties fall within acceptable bounds and when parameter variations are expressed in terms of readily measured system specifications. A method of satisfying these evaluation criteria is presented here.

This paper demonstrates the application of stochastic robustness analysis (i.e., determining the probability of unsatisfactory stability or performance resulting from expected parameter uncertainty) to solutions of the 1990 American Control Conference Benchmark Control Problem.[1] Stochastic robustness is seen to provide a useful, unifying analytical framework that is intuitive and has a direct, physical meaning.

Description of the Problem

The benchmark plant is a dual-mass/single-spring system with noncollocated sensor and actuator[1]; its state-space model is

$$\begin{bmatrix}\dot{x}_1\\ \dot{x}_2\\ \dot{x}_3\\ \dot{x}_4\end{bmatrix} = \begin{bmatrix}0 & 0 & 1 & 0\\ 0 & 0 & 0 & 1\\ -k/m_1 & k/m_1 & 0 & 0\\ k/m_2 & -k/m_2 & 0 & 0\end{bmatrix}\begin{bmatrix}x_1\\ x_2\\ x_3\\ x_4\end{bmatrix} + \begin{bmatrix}0\\ 0\\ 1/m_1\\ 0\end{bmatrix}u + \begin{bmatrix}0\\ 0\\ 0\\ 1/m_2\end{bmatrix}w \tag{1}$$

$$y = x_2 + v \tag{2}$$

$$z = x_2 \tag{3}$$

where x_1 and x_2 are the positions of the masses, x_3 and x_4 are their velocities, and u is a control force on m_1. The plant is disturbed by w on m_2, and the measurement of x_2 is corrupted by noise v in y. The corresponding actuator and disturbance input/output transfer functions are

$$\mathcal{TC}_{uy} = \frac{(k/m_1m_2)}{s^2\left[s^2 + k(m_1+m_2)/m_1m_2\right]} \tag{4}$$

$$\mathcal{TC}_{wy} = \frac{(1/m_2)(s^2 + k/m_1)}{s^2\left[s^2 + k(m_1+m_2)/m_1m_2\right]} \tag{5}$$

The plant has eigenvalues at $(\pm j\sqrt{k(m_1+m_2)/m_1m_2}, 0, 0)$ and is undamped. A single-input/single-output (SISO) controller must close its loop around $\mathcal{TC}_{uy}$, which has a pole-zero surplus of 4. The high-gain asymptote of at least one root lies in the right half plane for any SISO feedback compensator that has fewer than two surplus zeros. Because the open-loop roots are on the imaginary axis, the magnitudes of root departure angles must exceed 90 deg if marginal instability is to be avoided at low loop gain.

Three design problems are posed in Ref. 1. Benchmark problem 1 (BP-1) requires 1) a 15-s settling time for unit disturbance impulse and nominal mass-spring values ($m_1 = m_2 = k = 1$) and 2) closed-loop stability for fixed values of mass and $0.5 < k < 2$. The second problem, BP-2, replaces the unit-impulse disturbance by a sinusoidal disturbance with 0.5-rad/s frequency but unknown amplitude and phase. Asymptotic rejection of the signal should be achieved with a 20-s settling time for nominal masses and $0.5 < k < 2$. The third problem, BP-3, is like BP-1, except that m_1, m_2, and k are uncertain with mean values of 1 and unspecified bounds. A number of additional problem specifications are left to the discretion of the designer. For example, it is presumed that a noise model

Received May 14, 1991; revision received Oct. 4, 1991; accepted for publication Oct. 11, 1991.

*Professor, Department of Mechanical and Aerospace Engineering. Associate Fellow AIAA.

†Graduate Student, Department of Mechanical and Aerospace Engineering.

Research supported by government grant.

$v(t)$ would be considered, but details of the model are open. Subjective goals include achieving reasonable performance/stability robustness, minimizing controller effort, and minimizing controller complexity.

Design Solutions and Nominal Performance

Five papers containing design solutions appear in the American Control Conference Proceedings,[2-6] one paper became available after the conference,[7] and additional designs were obtained from the authors. The transfer functions for these controllers are presented in the Appendix. Fixed-order compensators achieving approximate loop-transfer recovery are motivated in Ref. 2, leading to designs A-C. An H_∞ plus $j\omega$-axis shifting approach is taken in Ref. 3, producing design D. Reference 4 uses nonlinear constrained optimization to produce design E. Structured covariance terms are added to the linear quadratic Gaussian (LQG) algebraic Riccati equations to generate design F in Ref. 5. Design G is a game-theoretic controller based on linear exponential Gaussian and H_∞ concepts and is discussed in Ref. 6. H_∞ controllers using the internal model principle are presented in Ref. 7 (designs H-J). G and J are designed to reject the sinusoidal disturbance (BP-2) rather than the unit impulse disturbance (BP-1). All but two of these designs (A and D) contain non-minimum-phase zeros. The benchmark criteria do not address command-input responses; hence, the initially reversed time response of systems with an odd number of non-minimum-phase zeros is not penalized. Design G has an even number of right-half-plane zeros, which would not produce reversed response.

The problem statement contains an ambiguity that could have affected the designers' interpretations of satisfactory response. Settling time is normally defined as an attribute of unit-step-function response. For example, Ogata[8] states that "The settling time is the time required for the response curve to reach and stay within a range about the final value of size specified by absolute percentage of the final value (usually 2% or 5%)." For a second-order system the 2% settling time can be precisely calculated as $4/\zeta\omega_n$, where ζ is the damping ratio and ω_n is the natural frequency of the oscillatory mode. However, Takahashi et al.[9] found that "Exact analytical expressions for ... settling time become prohibitively complicated for systems of order higher than two." The benchmark ambiguity is that the final value of a strictly stable impulse response (BP-1) is zero; hence, there is no steady-state value on which to base percentage response.

Nominal performance characteristics of the controllers are summarized in Table 1, which presents compensator numerator and denominator order (Num Ord and Den Ord), two definitions of settling time (T_S^* and T_S^{**}), maximum control usage (u_{max}) resulting from a unit w disturbance, gain margin (GM), phase margin (PM), output response to 0.5/rad/s sinusoidal disturbance (SR), and covariance of control response (U_{cov}) to measurement noise (v) with unit standard deviation. All compensators are proper (the number of zeros does not exceed the number of poles), but three (C, D, and E) are not strictly proper (the number of zeros equals the number of poles). Hence, designs A, B, and F-J can be classified as low-pass filters, whereas designs C-E do not roll off at high frequencies.

T_S^* portrays the settling time as the time for which x_2 is captured within a 0.1-unit envelope about its zero steady-state value, given an initial unit w disturbance impulse. T_S^{**} is based on the damping ratio and natural frequency of the dominant mode and is calculated as $4/\zeta\omega_n$. Neither of these definitions adheres to the conventional definition, but each has its merits. T_S^* is consistent with the BP-1 problem specification, in that it reflects a response to a unit w disturbance; however, it is amplitude dependent. T_S^{**} is independent of amplitude, but it is unrelated to the disturbance input and is not an accurate portrayal of the full system's settling time in response to a unit step input. Table 1 indicates that only three of the compensators satisfy a 15-s criterion by the first definition, whereas six compensators have settling times of ≤ 15.2 s by the second definition.

Four compensators use measurably more control than the others in responding to the disturbance. Increasing gain margin generally is accompanied by increasing phase margin for these 10 designs (Fig. 1), although the relationship is not monotonic. With the exception of design D, stability margins are less than the 8-dB/30-deg rules of thumb (e.g., Ref. 10) often suggested as design goals for SISO systems. Sinusoidal disturbance rejection of most controllers is similar, although design D's response is an order of magnitude smaller. Designs G and J, specifically intended to reject a 0.5-rad/s sinusoid, eliminate the disturbance completely in the steady state. (The settling time in achieving this response was not evaluated.) The noise-response covariance of the control is generally proportional to its peak disturbance-impulse response for strictly proper compensators. The three non-strictly proper compensators have infinite control covariance in response to continuous white measurement noise v (with infinite bandwidth).

Stochastic Robustness Analysis

Stochastic robustness analysis (SRA) is based on a statistical portrayal of parameter variations and their effects. If parameters take a finite number of discrete values, each with known

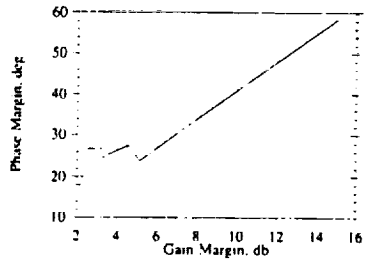

Fig. 1 Nominal gain and phase relationships of the 10 controllers.

Table 1 Nominal characteristics of 10 controllers

Design	Num Ord	Den Ord	T_S, s[a]	T_S, s[b]	u_{max} —	GM, db	PM, deg	SR, db	U_{cov} —
A	2	3	21.0	14.8	0.514	2.56	26.7	10.1	6.30
B	2	3	19.5	15.2	0.469	3.27	26.8	13.2	13.02
C	2	2	19.7	15.2	0.468	3.27	26.5	13.3	∞
D	4	4	9.9	8.8	297.8	15.10	58.7	1.47	∞
E	2	2	18.2	8.01	0.884	2.39	22.0	17.1	∞
F	3	4	13.7	22.0	2.397	5.15	23.8	13.4	6×10^4
G	5	8	31.3	35.7	1.458	3.61	25.4	$-\infty$	173.5
H	3	4	14.9	11.9	0.574	3.28	24.5	14.9	2.48
I	3	4	17.8	17.2	0.416	4.56	27.5	13.3	0.95
J	5	6	43.2	23.8	1.047	2.14	17.5	$-\infty$	77.42

[a] *Defined for 0.1-unit response envelope for unit-impulse w.
[b] **Defined by $4/\zeta\omega_n$ (provided by B. Wie).

or estimated probability, the analysis can be based on a finite number of function evaluations, and the probabilistic result is exact (within the accuracy and precision of problem modeling). If the parameters are continuous or the number of finite combinations is too large for practical computation, Monte Carlo evaluation can be used to estimate probabilities within arbitrarily small confidence intervals. If a binary judgment can be made of function values (e.g., satisfactory/unsatisfactory or stable/unstable), then the corresponding probability distribution is binomial, and confidence intervals are readily estimated from the number of function evaluations (e.g., Ref. 11). Further details of SRA can be found in Refs. 12-17.

Test Cases for the Benchmark Problem

Uncertain parameters are assumed to have continuous, bounded, uniform, and uncorrelated probability distributions for this analysis. (The original problem identifies uncertain parameters and their bounds, making no statement about distributions.[1]) Three increasingly demanding sets of parameter uncertainties are used to test the controllers. The first two are specified in Ref. 1, and the third is new.

Problem E-1: $0.5 < k < 2$, all other parameters take nominal values, as in BP-1 and BP-2.

Problem E-2: $0.5 < k < 2$, $0.5 < m_1 < 1.5$, and $0.5 < m_2 < 1.5$, as in BP-3. Reference 1 does not specify limits on m_1 and m_2; values of $\pm 50\%$ are adopted here.

Problem E-3: Same as E-2; in addition, $0 < c < 0.1$, $0.9 < f < 1.1$, and $0.001 < \tau < 0.4$ s, where c represents internal damping between the masses; f is loop-gain uncertainty due to multiplicative variation in observation, control gain, or actuator effectiveness; and τ is the time constant for a first-order lag between controller command and actuator response. Uncertainty in the damping ratio c increases open-loop damping, and the time lag is always greater than the nominal value of zero.

With all six parameters, the state-space model for E-3 becomes

$$\dot{x}' = F'x' + G'u_c + L'w \tag{6}$$

where x' is defined as $[x_1\ x_2\ x_3\ x_4\ u]^T$, and

$$F' = \begin{bmatrix} 0 & 0 & 1 & 0 & 0 \\ 0 & 0 & 0 & 1 & 0 \\ -k/m_1 & k/m_1 & -c/m_1 & c/m_1 & f/m_1 \\ k/m_2 & -k/m_2 & c/m_2 & -c/m_2 & 0 \\ 0 & 0 & 0 & 0 & -1/\tau \end{bmatrix} \tag{7}$$

$$G' = [0\ \ 0\ \ 0\ \ 0\ \ 1/\tau]^T \tag{8}$$

$$L' = [0\ \ 0\ \ 0\ \ 1/m_2\ \ 0]^T \tag{9}$$

The compensators are modeled by

$$\dot{x}_c = Ax_c + By \tag{10}$$

$$u_c = Cx_c + Dy \tag{11}$$

where x_c is the compensator state; u_c is the actuator command; A, B, C, and D are the compensator matrices; and y is x_2.

Performance Metrics for the Benchmark Problem

Robustness is best characterized by problem-dependent metrics that have a direct bearing on the measurable stability and performance of the system. Here, they portray the likelihood that classical stability bounds will be exceeded, that settling time will not be achieved, and that control usage will exceed acceptable values. For demonstration of SRA, parameter uncertainties are represented by uniform distributions within arbitrary (but reasonable) bounds. In practical application, the control-system designer would have similar, problem-specific specifications to meet.

Each of the following probabilistic performance metrics has a binomial distribution and is estimated using Monte Carlo evaluation. Uniform, bounded parameters are calculated by random-number generators according to the specifications of the previous section. The associated binomial confidence level depends on the number of evaluations and the value of the probability estimate.[13] Each estimate is the result of 20,000 evaluations; for a probability estimate of 0.1, the 95% confidence interval would be ± 0.004. The performance metrics are:

1) P_I: Probability of instability. This probability portrays the likelihood that parameter variations force at least one closed-loop root into the right half plane.

2) P_{T_s}: Probability of settling-time exceedance. This probability is derived from a time-history calculation with a unit-impulse w input (i.e., based on T_S^*) and estimates the likelihood that the actual response of z will fall outside a ± 0.1-unit envelope after 15 s.

3) P_u: Probability of control limit exceedance. This probability corresponds to the requirement in Ref. 1 to minimize controller effort. It is the probability that peak actuator displacement will exceed a saturation limit in response to a unit disturbance (w) impulse. The saturation limit was chosen to be one unit for this analysis.

4) P_f: Probability of unsatisfactory sinusoidal disturbance rejection. This probability involves the likelihood that the amplitude of steady-state z response exceeds one unit with a unit sinusoidal disturbance at 0.5 rad/s.

Computation times indicate that current workstations are fast enough to execute practical SRA, and massively parallel computers could provide interactive turnaround. For the typical closed-loop system considered here, roughly 900 sets of eigenvalues were generated per minute per million floating-point operations per sec (MFLOP). This is drawn from compiled Pascal code executed on a 0.9-MFLOP Silicon Graphics 4D/20 workstation. The complete evaluation was computed at a rate of 30 sets/min/MFLOP using MATLAB on a Macintosh IIx computer. At these rates, a 5000-MFLOP parallel computer (e.g., 64K CM-2 Connection Machine) would evaluate 20,000 sets of eigenvalues in 0.25 s, and the full evaluation would take about three times longer.

Results of the Analysis

The results of the SRA indicate a wide range of characteristics in the 10 controllers. This reflects varying emphasis in satisfying the problem specifications, as well as significant differences in compensator order and design philosophy. It should be emphasized that none of the controllers was designed for the express purpose of satisfying SRA criteria, and it is likely that each design approach could be fine-tuned to produce better results than those shown here. Using criteria that have high engineering significance, SRA provides a "level playing field" on which to judge the robustness of controllers that were designed by alternative methods. Tables 2-4 present results, with maximum probabilities for each evaluation problem indicated by bold letters and minimum values underlined.

Probability of Instability

For the least uncertain case (E-1), over half of the controllers are estimated to have zero probability of instability, whereas design A has a 16% likelihood of instability (Table 2). With increasing parameter uncertainty (E-2 and E-3), all controllers have nonzero P_I. The probability of design A is essentially unchanged, and design J becomes the controller most likely to be unstable.

It is interesting to compare the probabilities of instability on the bases of gain and phase margins, quantities often assumed to indicate the robustness of SISO systems. Figures 2 and 3 demonstrate that nominal values of GM and PM are *not* good predictors of P_I. (Note that these bar charts present results for the 10 compensators; hence, GM and PM are not evenly dis-

Table 2 Probability of instability

Design	E-1	E-2	E-3
A	**0.160**	0.159	0.165
B	0.023	0.042	0.039
C	0.021	0.040	0.041
D	0.000	0.004	0.059
E	0.000	0.097	0.125
F	0.000	0.119	0.224
G	0.000	0.203	0.232
H	0.000	0.046	0.099
I	0.000	0.013	0.029
J	0.039	**0.237**	**0.245**

Table 3 Probability of settling-time violation

Design	E-1	E-2	E-3
A	0.971	0.962	0.793
B	**1.000**	0.969	0.963
C	**1.000**	0.968	0.874
D	0.000	0.004	0.072
E	**1.000**	**1.000**	0.999
F	0.633	0.859	0.967
G	**1.000**	0.999	**1.000**
H	0.742	0.909	0.986
I	0.756	0.918	0.986
J	**1.000**	**1.000**	0.968

Table 4 Probability of control-limit exceedance

Design	E-1	E-2	E-3
A	0.160	0.159	0.165
B	0.023	0.043	0.047
C	0.021	0.041	0.041
D	**1.000**	**1.000**	**1.000**
E	0.000	0.391	0.409
F	**1.000**	**1.000**	**1.000**
G	**1.000**	0.886	0.889
H	0.000	0.133	0.162
I	0.000	0.023	0.030
J	0.857	0.542	0.527

tributed.) In most cases, increasing parameter uncertainty increases P_I, but there are no consistent trends with GM and PM. Parameter variations have complex effects on the *shape* of each controller's Nyquist plot, and these effects cannot be portrayed simply by changing loop gain or phase angle.

This result brings into question the utility of transfer-function/return-difference-matrix singular values as measures of the stability robustness of multi-input/multi-output (MIMO) systems. MIMO singular-value analysis is loosely equivalent to SISO gain-margin analysis (e.g., Ref. 18). Arbitrary, real parameter variations have complicated effects on the frequency distributions of MIMO singular values, changing their shapes as well as their magnitudes. Unless the frequency distributions of *nominal* MIMO norms retain their shapes under parameter variation (or follow some predictable pattern), the relationships of nominal maximum or minimum values to allowable bounds tells little about stability robustness. Norm bounds can be reliably evaluated only by considering the norms of *perturbed* systems.

A higher compensation order does not necessarily improve robustness (Tables 1 and 2). The compensators with the most stability robustness are fourth order, and the next most robust controllers are second and third order. Increased nominal control usage, either as a consequence of a disturbance impulse or measurement noise, generally corresponds to decreased stability robustness, although design D provides a significant exception.

Probability of Settling-Time Violation

All but three of the controllers (D, F, and H) exceed the 15-s settling-time objective (defined by T_5^*) in the nominal case (Table 1); hence, it is not surprising that the probability of settling-time violation with parameter uncertainty is high as well (Table 3). Design D provides a notable exception: Its nominal T_5^* is 9.9 s, and P_{T_s} is small for all three evaluation cases. For problem E-1, half of the controllers violate the goal all the time, but two of the controllers with nominal T_5^* above 15 s (H and I) have a considerable likelihood (25%) of satisfying the objective when the spring-constant uncertainty is considered. Further uncertainty (problems E-2 and E-3) reduces the probability of settling-time violation for more controllers, illustrating the counterintuitive result that the effects of uncertainty are not always unfavorable.

Probability of Control Limit Exceedance

The probability of excessive control response to disturbance impulse P_u is shown in Table 4. Over half of the nominal responses are within the u_{max} criterion chosen for this analysis (Table 1). Furthermore, there is an identifiable trend in the relationship between u_{max} and P_u (Fig. 4). Several controllers (E, H, and I) have zero probability of violating this criterion for problem E-1, and designs B, C, and I retain low values of P_u for all three problems. Designs D and F have 100% P_u in all three cases, which is traceable to very high nominal control usage. Once again, nominally marginal cases (G and J, the two controllers designed for rejection of the sinusoid) exhibit reduced probability of exceedance for problems E-2 and E-3. From Eq. (1), increased m_1 and m_2 decrease the effects of u and w, and added damping (c) and first-order lag (τ) reduce control peaks in some cases, reducing the probability of high control levels.

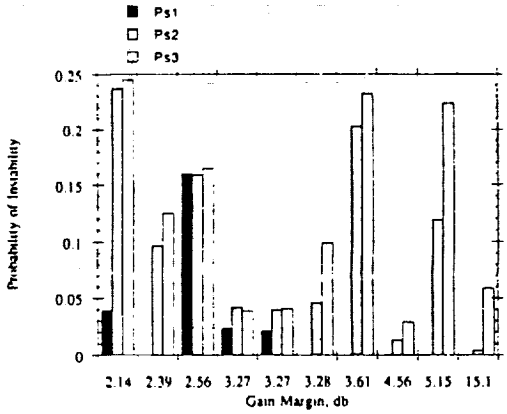

Fig. 2 Probability of instability vs gain margin for three evaluation problems.

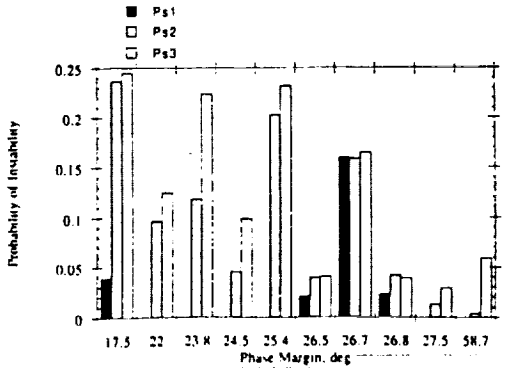

Fig. 3 Probability of instability vs phase margin for three evaluation problems.

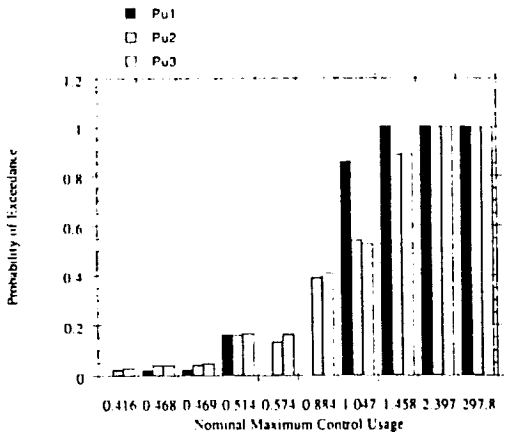

Fig. 4 Probability of control-limit exceedance vs nominal maximum control response to a disturbance impulse.

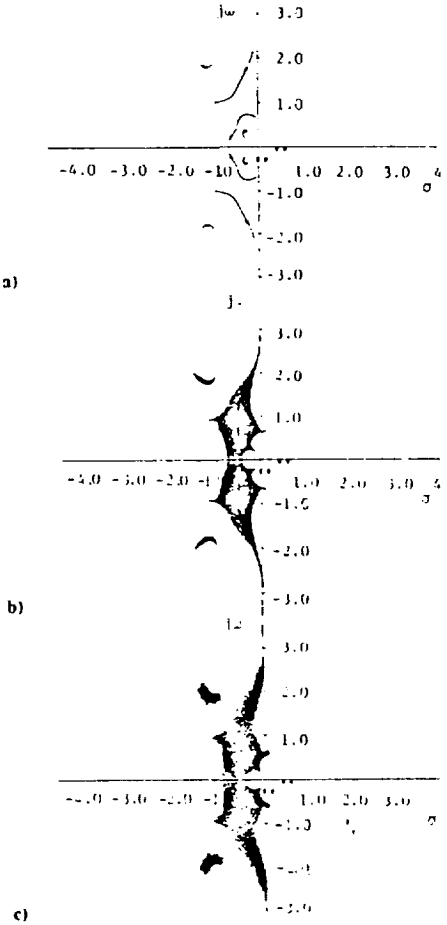

Fig. 5 Stochastic root locus of design H (scatter plot): a) problem E-1; b) problem E-2; c) problem E-3.

Sinusoidal Response Characteristics

When 0 dB is chosen as an upper response limit, the two controllers designed to reject the sinusoid (G and J) do so perfectly ($P_f = 0$), whereas all the others exceed the limit all the time. The transfer functions (Appendix) show that designs G and J effectively "notch" the 0.5-rad/s disturbance-input frequency to produce these results. Without notch filters the remaining controllers cannot give special attention to discrete-frequency inputs, and their frequency response of −0.5 rad/s always exceeds 0 dB. If the frequency of the sinusoidal disturbance were uncertain, the notch filters could be less effective, but there would be little change in the response of the other controllers.

Stochastic Root Loci and Parametric Histograms

Graphical results give insight into the nature and causes of possible instability. The stochastic root locus is an s-plane plot of the eigenvalues that result from each Monte Carlo evaluation, expressed either as a two-dimensional scatter plot of closed-loop roots or an oblique three-dimensional view of the density of roots within subspaces of the s plane.[13] The former plot is easily generated from the calculations, and the latter has the advantage of showing the distribution along the real axis.[17] In addition, histograms of the parameters associated with instability can be related to origins of the problem.

Scatter plots for design H show the progression of eigenvalue uncertainty from problem E-1 to E-3 (Fig. 5). For prob-

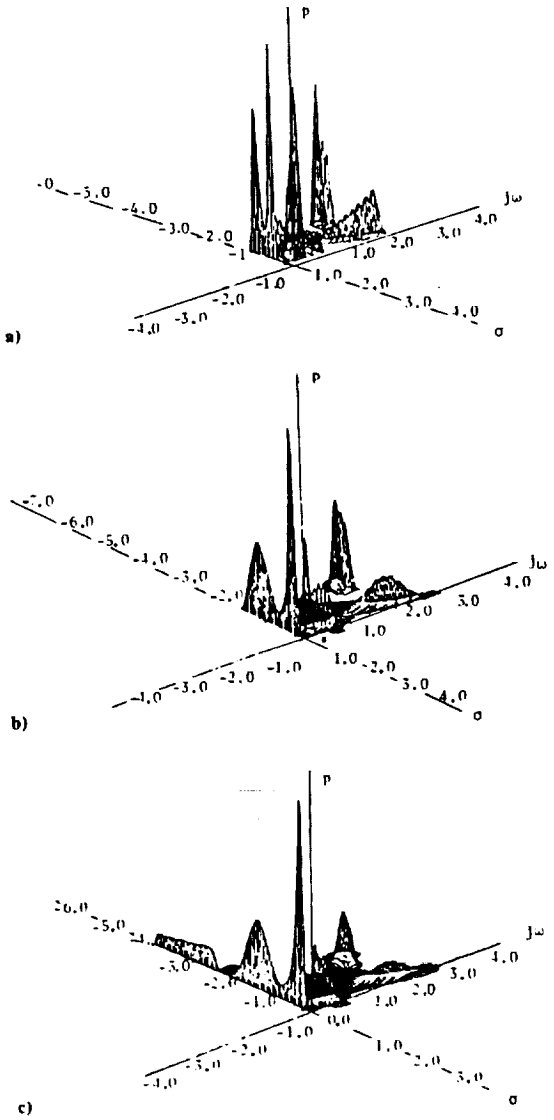

Fig. 6 Stochastic root locus of design H (three-dimensional view): a) problem E-1; b) problem E-2; c) problem E-3.

lem E-1 only a single parameter varies (the spring constant k). The distribution follows the conventional root locus (with nominal closed-loop locations indicated by $\times$), although the density of roots varies along the curves. The pairs of roots near the origin are most closely associated with the plant, whereas the higher-frequency roots are compensator modes. None of the root loci extend into the right half plane, and P_I is zero (Table 2). Three parameters vary in problem E-2, and the stochastic root locus becomes an areal distribution of roots, some of which extend into the right half plane (Fig. 5b). Because the parameter variations are bounded, there are crisp edges to the distributions. The unstable cusps at 0.6 and 2.6 rad/s can be associated with plant and controller modes. Further parametric uncertainty (problem E-3) broadens the distributions and increases the probability of instability.

The same information is presented in unsmoothed three-dimensional form in Fig. 6 (upper half plane only), which shows the distribution of real roots as well. The three-dimensional representation is especially effective when displayed on a graphics workstation that allows the viewpoint to "fly around" the distribution.

To see which parameter values are associated with instability, the values are recorded whenever the system is found to be unstable. These values are collected in intervals, the number of values in each interval is counted, and the resulting histogram provides an estimate of the conditional probability density function for each parameter. If a parameter has little effect on stability, then the histogram should show the same distribution as produced by the random number generator—in this case, a uniform distribution. If particular values of the parameter increase the probability of instability, the histogram has higher values in that region.

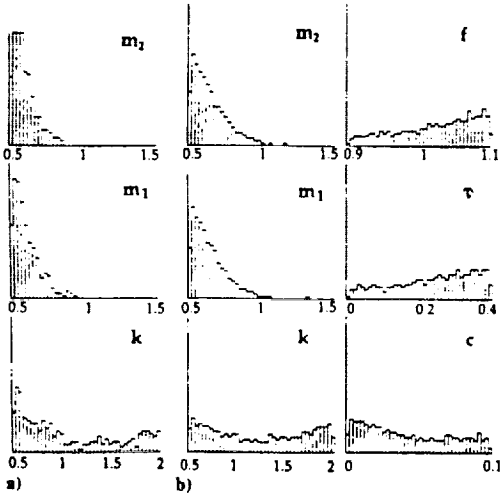

Fig. 7 Parameter histograms for all unstable cases, design H: a) problem E-1; b) problem E-3.

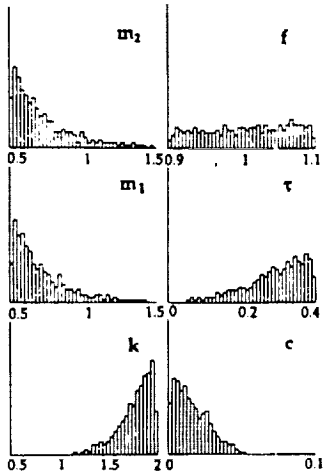

Fig. 8 Parameter histograms for high-frequency unstable cases, design H, problem E-3.

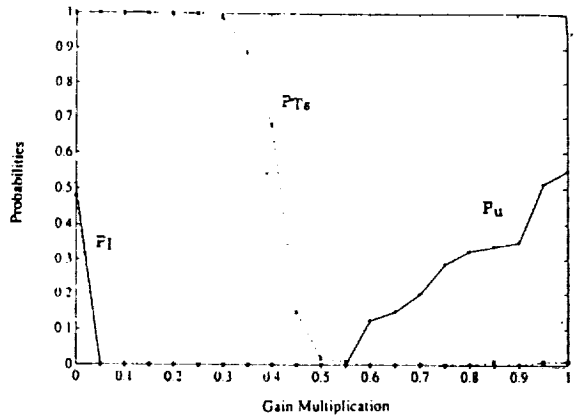

Fig. 9 Effect of reducing design D loop gain on P_I, P_{T_s}, and P_u.

For design H and problem E-2, instability often occurs when the masses have low values but never occurs with high values (Fig. 7a). Low mass values increased the probability of instability for all the designs. Extreme values of the spring constant also are associated with instability, low values having the edge in this example.

For problem E-3 (Fig. 7b), the distributions become less crisp, as otherwise unstable values of mass can be stabilized by damping and otherwise stable values of mass can be destabilized by increased loop gain or first-order lag. The spring constant shows a slight bimodal distribution due to the two modes of instability with roots of approximately 0.6 or 2.6 rad/s. This can be seen by recording the parameter values only when the system is found to be unstable *and* the unstable roots have a high frequency. The resulting histograms (Fig. 8) show that there are unstable high-frequency roots only if the spring constant is high and the damping is low. With increased damping, there is no high-frequency instability.

These results can be used in three ways. The probability of instability could be reduced if it were possible to ensure that the plant parameters did not move into the areas that are found to cause problems. This might be the result of improved quality assurance on the important parameters or by shifting the mean of the parameter variation. If it is not possible to affect the actual parameter variations, then the control system could be redesigned using the problematic values of parameters as nominal values. For example, the control system could be redesigned using nominal values of 0.7 for the masses.

A third use of the distributions can occur if one of the varying parameters represents a control design parameter. For instance, if the loop gain f were treated as a design variable, then it is clear that attenuating the gain would reduce the probability of instability. This alternative is demonstrated using design D. It has been seen that design D had generally good robustness but very high actuator use. Peak actuator usage can be reduced by reducing the loop gain, and the effect of gain attenuation on robustness subject to problem E-2 is shown in Fig. 9. For this analysis, only 100 Monte Carlo evaluations were carried out per design point, but the results show clear trends. As the gain is reduced, the probability of control saturation is reduced without significant increase in P_I or P_{T_s} until the attenuation reaches 0.6, when P_{T_s} begins to increase. Reducing the gain further produces a clear trade-

off between the probabilities of control saturation and settling-time violation. References 19 and 20 present similar methods of control system design based on search and statistical evaluation.

Conclusions

Stochastic robustness analysis of 10 controllers designed for the ACC Benchmark Control Problem provides useful quantification of stability and performance sensitivities to parameter variations. The SRA method is flexible and can be tailored to the design requirements and system specifications of particular control problems. Qualitative selection of the best controller depends on the relative importance of several metrics, which are readily described in a probabilistic framework.

Several conclusions can be drawn from this analysis. The analysis shows that gain and phase margins are not good predictors of the relative stability robustness of different SISO controllers, because robustness is tied closely to the actual plant uncertainties and their effects on (implied) Nyquist contours. This result implies that robustness analyses based on singular-value analysis of MIMO systems may have similar limitations. Nominal settling time did not give a good indication of the likelihood of exceeding settling-time limit, principally because most nominal values already exceeded the limit. Although this result may be an artifact of the settling-time definition (T_S^*), it reveals the counterintuitive result that uncertainty may improve the probability of remaining within a predefined limit. The relationship between maximum control response to a disturbance impulse and the probability of exceeding a control limit is more direct, as most nominal values were about half the limit value. Stochastic root loci and parameter histograms provide insight about the likely positions of the closed-loop roots and the parameter variations that lead to instability, and they suggest ways of improving plant and controller design.

Appendix: Transfer Functions of the Ten Compensators

Design A:

$$\frac{40.42(s+2.388)(s+0.350)}{(s+163.77)\left[s^2+2(0.501)(0.924)s+(0.924)^2\right]}$$

Design B:

$$\frac{42.78(s-1.306)(s+0.1988)}{(s+73.073)\left[s^2+2(0.502)(1.182)s+(1.182)^2\right]}$$

Design C:

$$\frac{0.599(s-1.253)(s+0.1988)}{\left[s^2+2(0.502)(1.182)s+(1.182)^2\right]}$$

Design D:

$$\frac{19881(s+100)(s+0.212)\left[s^2+2(0.173)(0.733)s+(0.733)^2\right]}{\left[s^2+2(0.997)(51.16)s+(51.16)^2\right]\left[s^2+2(0.838)(16.44)s+(16.44)^2\right]}$$

Design E:

$$\frac{5.369(s-0.348)(s+0.0929)}{\left[s^2+2(0.832)(2.21)s+(2.21)^2\right]}$$

Design F

$$\frac{2246.3(s+0.237)\left[s^2-2(0.32)(1.064)s+(1.064)^2\right]}{(s+33.19)(s+11.79)\left[s^2+2(0.90)(2.75)s+(2.75)^2\right]}$$

Design G:

$$\frac{4430(s+0.08)(s-0.44)(s-2.83)\left[s^2-2(0.102)(0.49)s+(0.49)^2\right]}{\left\{\left[s^2+2(0.70)(11.17)s+(11.17)^2\right]\left[s^2+2(0.89)(3.67)s+(3.67)^2\right]\left[s^2+2(0.29)(3.11)s+(3.11)^2\right]\left[s^2+(0.5)^2\right]\right\}}$$

Design H:

$$\frac{2.13(s+0.145)(s-0.98)(s+3.43)}{\left[s^2+2(0.82)(1.59)s+(1.59)^2\right]\left[s^2+2(0.46)(2.24)s+(2.24)^2\right]}$$

Design I:

$$\frac{16.1(s+0.134)(s-1.174)(s+1.46)}{\left[s^2+2(0.82)(1.05)s+(1.05)^2\right]\left[s^2+2(0.5)(2.18)s+(2.18)^2\right]}$$

Design J:

$$\frac{51.47(s+0.06)(s-0.21)(s+5.41)\left[s^2-2(0.07)(0.51)s+(0.51)^2\right]}{\left[s^2+2(0.72)(2.05)s+(2.05)^2\right]\left[s^2+2(0.68)(5.21)s+(5.21)^2\right]\left[s^2+(0.5)^2\right]}$$

Stochastic Prediction Techniques for Wind Shear Hazard Assessment

D. Alexander Stratton* and Robert F. Stengel†
Princeton University, Princeton, New Jersey 08540

The threat of low-altitude wind shear has prompted development of aircraft-based sensors that measure winds directly on an aircraft's intended flight path. Measurements from these devices are subject to turbulence inputs and measurement error, as well as to the underlying wind profile. In this paper stochastic estimators are developed to process onboard Doppler sensor measurements, producing optimal estimates of the winds. A stochastic prediction technique determines the level of aircraft energy performance from the wind estimates. Aircraft performance degradation algorithms presented are based on optimal estimation techniques. The prediction algorithm must balance wind shear detection performance and turbulence rejection capability, as illustrated in simulations of microburst wind shear and severe turbulence environments.

Introduction

STRONG variable winds in the airport vicinity can cause unacceptable deviation of aircraft from their intended flight path. Known as low-altitude wind shear, this threat has caused at least 24 aviation accidents in the last 25 years.[1] Efforts to promote the avoidance of severe wind shear have focused on improving flight crew training programs,[2] understanding the meteorology of wind shear,[3-5] and developing technology to detect wind shear in the terminal area. Ground-based sensor systems to measure airport-vicinity winds are being developed and installed at major airports,[6,7] along with techniques to automatically identify a wind shear and predict its formation.[8-10] Sensors to detect wind-shear-induced flight-path deviations are being installed on aircraft,[11,12] and forward-looking sensors to detect wind shear in front of the aircraft also are under development.[13-15] Interpretation of this information in the cockpit is a topic of current research.

As the amount of available information grows, accurate interpretation of the information by flight crews becomes more challenging, particularly during periods of high workload. Artificial intelligence technology provides a basis for a cockpit aid to assist flight crews in avoiding low-altitude wind shear. An expert system, the Wind Shear Safety Advisor,[16] depicted schematically in Fig. 1, will operate in real time, accepting evidence from onboard and ground-based sources, perhaps facilitated by a direct data link (represented by a dotted line in Fig. 1). The goal of this system is to increase flight crew situation awareness and decision reliability by summarizing information from a variety of information sources.

In the absence of direct measurements of the winds, a decision to avoid wind shear must be based on discrete alerts from wind shear detection systems and meteorological evidence. Various levels of reliability associated with this indirect evidence complicate the risk assessment process. A probabilistic model of this process has been developed that incorporates statistics from meteorological studies and reliability statistics for wind-shear-alerting systems.[17] The model can manage the uncertainty associated with indirect evidence, providing meaningful estimates of risk.

If onboard measurements of the winds were available, a hazardous level of wind shear could be identified by determining whether the level of some hazard metric, based on the wind measurements, exceeds a threshold. Hazard metrics considered previously include maximum horizontal winds[3] and F-factor,[14] which relates wind shear to aircraft performance. Computation of the hazard level is complicated by uncertainty surrounding the wind measurements, including turbulence and measurement errors. In this paper Kalman filters are developed to produce optimal wind estimates from onboard wind sensors, based on a stochastic wind model. These algorithms are demonstrated in a simulated microburst wind shear environment.

From the wind estimates, predictions of the aircraft's performance degradation can be made using stochastic prediction techniques.[18,19] In addition to the predictions themselves, these techniques produce measures of the possible error in the predictions due to turbulence and limitations of the measurement devices. In this paper a Kalman-filter-based prediction technique to predict F-factor and aircraft performance degradation is demonstrated in simulated microburst wind shear encounter. The response characteristics of the prediction technique must provide significant response to severe wind shear and limited response to turbulence. In this paper stochastic prediction techniques with different design parameters are demonstrated in a simulated microburst wind shear and severe turbulence environments.

Probabilistic Reasoning in Artificial Intelligence

The power of an intelligent system rests in its ability to produce meaningful conclusions by reasoning, i.e., by applying knowledge stored in the system to available evidence. In probabilistic models of reasoning, knowledge is stored in the form of probabilities, and Bayes's rule[20] and the axioms of probability[21] are used to condition these probabilities on evidence. When several pieces of evidence are supplied, the application of Bayes's rule is complicated by dependencies between pieces of evidence. A structure to these dependencies must be provided for efficient reasoning. In Bayesian network representation[22] a graphical representation provides this structure, such as the one for wind shear avoidance graphed in Fig. 2. Nodes in the diagram represent discrete random variables, and the links between them represent sets of conditional probabilities used during reasoning. The network representation enables efficient probabilistic reasoning because all of the dependencies between variables are specified by the links.

The network of Fig. 2 was developed using guidelines for wind shear avoidance presented in the FAA's Windshear Training Aid document,[2] which was written by a team from

Received Feb. 12, 1991; revision received Sept. 12, 1991; accepted for publication Oct. 6, 1991.

*Research Assistant, Department of Mechanical and Aerospace Engineering. Member AIAA.

†Professor, Department of Mechanical and Aerospace Engineering. Associate Fellow AIAA.

Research supported by government grant.

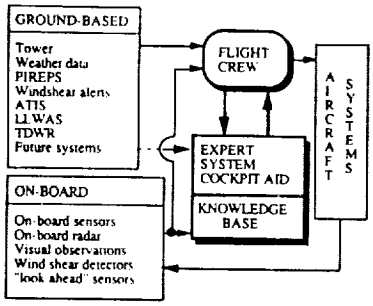

Fig. 1 Wind shear safety advisor schematic diagram.

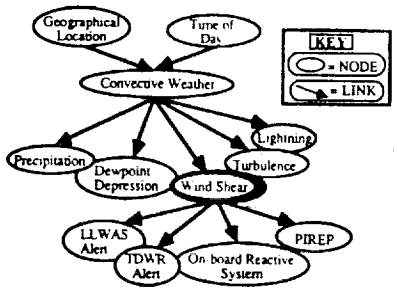

Fig. 2 Graphical representation of a Bayesian network for wind shear avoidance.

the airframe industry with the support of airlines, the government, and academia. The network model incorporates statistical results from the NIMROD,[3] JAWS,[3,4] and FLOWS[5] studies and for the enhanced Low-Level Windshear Alert System (LLWAS) evaluation.[7] Demonstrations of the network[17] show that it can approximate the subjective judgments required to establish the possible presence of wind shear.

A probabilistic model establishes a scientific basis for the Windshear Training Aid avoidance guidelines. Since the completion of the Windshear Training Aid, a variety of new ground-based and airborne wind shear detection systems are being devleoped, such as the Terminal Doppler Weather Radar (TDWR) system. The probabilistic model can be expanded to include statistics from new detection systems established during their evaluation. New knowledge gained from meteorological studies, such as geographical variation of wind shear frequency, can also be included.

Kalman Filter Development for Doppler Wind Measurements

Airborne sensor technology with the capability to detect wind shear in front of the aircraft is currently under development, including Doppler radar,[13] Doppler lidar,[14] and infrared[15] technology. Doppler devices measure a shift in frequency of radar or light waves emitted along a radial line, measuring the component of wind velocity parallel to that line. Operational devices could provide measurements of head winds or tail winds at a series of locations along the aircraft's intended approach or takeoff path. For example, airborne Doppler radars could provide measurements spaced at ~500-ft intervals over a range of 3-5 miles, spanning 50-100 s of flight at approach speed.[13] This sequence of measurements contains the effect of turbulence and is corrupted by measurement noise as well. A bank of Kalman filters can improve the accuracy of hazard estimates based on successive measurement sequences, minimizing measurement noise and accounting for correlation in the wind field using a stochastic model.

As the aircraft travels down the flight path measurements in successive sequences are offset by a distance d (Fig. 3), which is assumed to be small relative to the distance between adjacent range gates L. At a given time, a sequence of measurements is obtained. Each member of this sequence represents the average value of the radial wind component in an interval of length L at that time.

A first-order Markov model for the turbulent winds can be based on the Dryden power spectrum for horizontal turbulence, given by Ref. 23 as

$$\Phi_u(\omega) = \left(\frac{2L_u\sigma_u^2}{\pi}\right)\frac{1}{\left[1+(L_u\omega)^2\right]} \tag{1}$$

Parameters of this model include the turbulence scale length L_u and the root-mean-square turbulence amplitude σ_u. The corresponding discrete Markov sequence is

$$w_{t_k} = \exp(-d_u)\,w_{t_{k-1}} + \sqrt{1-\exp(-2d_u)}\,\eta_{k-1} \tag{2}$$

where d_u is the ratio of d to L_u. The η is a normally-distributed white noise sequence with mean and variance:

$$E[\eta_k] = 0 \tag{3}$$

$$E[\eta_k^2] = \sigma_u^2/\pi \tag{4}$$

This model uses the discrete white noise sequence η to approximate the integrated effect of continuous white noise. Figure 4 presents the autocovariance function associated with Eq. (1), along with the autocovariance function of the sequence of Eq. (2), indicating the agreement of the turbulence models.

With the assumption that measurement noise is superimposed on the radial wind components, the measurement at range gate j during measurement sequence k, z_{jk} can be related

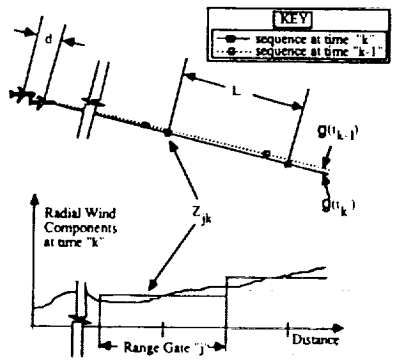

Fig. 3 Forward-look sensor measurement process.

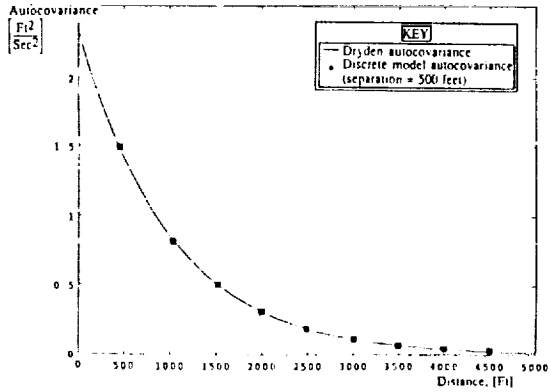

Fig. 4 Comparison of Dryden turbulence spectrum autocovariance function and autocovariance function of discrete turbulence model.

to the corresponding scalar radial wind component by the relationship

$$z_{jk} = w_{r_{jk}} + n_{jk} + V_{I_k} \tag{5}$$

This can be rewritten as

$$\tilde{z}_{jk} = w_{r_{jk}} + \tilde{n}_{jk} \tag{6}$$

where V_I is the aircraft's inertial speed at the time of measurement sequence k, and $\tilde{z}_{jk}$ has this bias subtracted out. Error in the inertial speed estimate, n_{V_I}, which is made from onboard measurements, is added to n_{jk} to produce $\tilde{n}_{jk}$:

$$\tilde{n}_{jk} = n_{jk} + n_{V_I} \tag{7}$$

The measurement error $\tilde{n}$ is assumed to be a zero-mean, normally distributed white noise sequence, with a known constant standard deviation σ_n.

With the aforementioned assumptions, an estimator dedicated to each range gate can be constructed in the form of a Kalman filter. From the measurement $\tilde{z}_{jk}$, each Kalman filter constructs an estimate $\hat{w}_{r_{jk}}(+)$ and a variance $p_{jk}(+)$, which is a measure of the uncertainty in $\hat{w}_{r_{jk}}(+)$, in three steps. First, the state estimate and variance form the previous measurement sequence, $\hat{w}_{r_{jk-1}}(+)$ and $p_{jk-1}(+)$, are extrapolated according to

$$\hat{w}_{r_{jk}}(-) = \exp(-d_u)\hat{w}_{r_{jk-1}}(+) \tag{8}$$

$$p_{jk}(-) = \exp(-2d_u)p_{jk-1}(+) + \left[1 - \exp(-2d_u)\right]\sigma_u^2/\pi \tag{9}$$

Equation (8) is obtained by taking the expected value of Eq. (2). Note that Eq. (9) is an approximation to the integrated effects of continuous white noise. Next, the extrapolated variance $p_{jk}(-)$ is used to compute a gain K_{jk}:

$$K_{jk} = \frac{p_{jk}(-)}{p_{jk}(-) + \sigma_n^2} \tag{10}$$

Finally, the post-update wind estimate and variance are computed:

$$\hat{w}_{r_{jk}}(+) = \hat{w}_{r_{jk}}(-) + K_{jk}\left[\tilde{z}_{jk} - \hat{w}_{r_{jk}}(-)\right] \tag{11}$$

$$p_{jk}(+) = \left[p_{jk}(-) + \sigma_n^2\right] / \left[p_{jk}(-)\sigma_n^2\right] \tag{12}$$

The Kalman filters compute a weighted average of the wind measurements obtained at each range gate, compensating for the movement of the sensor platform by making an assumption of frozen Dryden turbulence in the interval between the measurements. Wind shear estimates are updated at each measurement step, compensating for turbulence and weighing current and prior information according to its relative uncertainty. Because each range gate's state estimator is decoupled from the others, the computation could be performed on a set of identical processors running in parallel. This decoupling is achieved as a consequence of the Markov property of the wind model: the probability distribution at a given wind state $w_{r_{jk}}$ is conditionally independent of $w_{r_{j-1,k}}$ given the closer state $w_{r_{jk-1}}$. This assumption could be relaxed, coupling adjacent states or larger groups of states together with a corresponding increase in computational complexity.

Prior state estimates and variances are required to initialize each filter. This may be accomplished by applying a separate initialization Kalman filter to the first sequence of wind measurements. This filter is initialized with an onboard wind estimate and variance at the aircraft's location, perhaps from a Kalman filter processing onboard sensor measurements. An initial sequence of wind measurements from the forward-looking sensors is then processed to initialize the state and variance of each Kalman filter. The initialization Kalman filter takes the same form as Eqs. (8-12), except that the distance between range gates L is used as the distance between measurements d.

Hazard Metrics and Stochastic Prediction

The detection of the presence of a wind shear can be based on the output of the stochastic estimators. A reasonable approach to detecting wind shear is to predict whether the level of some hazard metric based on the wind estimates will exceed a threshold. The F-factor hazard metric relates wind shear to aircraft air-referenced specific energy rate, which is defined by

$$\frac{dE_s}{dt}(t) = \left(\frac{V_a}{g}\right)\frac{dV_a}{dt} + \frac{dh}{dt} \tag{13}$$

where V_a is the airspeed, h is aircraft altitude, and g is the gravitational constant. Using longitudinal aircraft equations of motion and assuming small flight-path angles, it can be shown[14] that

$$\frac{dE_s}{dt}(t) = \frac{(T - D)V_a}{W} - \mathcal{F}(t)V_a \tag{14}$$

where T is thrust, D is drag, and W is aircraft weight. $\mathcal{F}(t)$ is the F-factor, defined as

$$\mathcal{F}(t) = \left(\frac{1}{g}\right)\frac{dw_s}{dt}(t) - \frac{w_h(t)}{V_a} \tag{15}$$

where $w_s(t)$ is the wind component in the inertial horizontal direction, and $w_h(t)$ is the vertical wind component. For small flight-path angles, the radial wind components are approximately the same as the longitudinal horizontal wind components. Wind shear effects enter Eq. (14) in three ways: 1) by changing the airspeed, 2) by altering the drag, and 3) directly through $\mathcal{F}(t)$. For conditions typical of jet transport flight through severe wind shear, only the direct impact of $\mathcal{F}(t)$ is significant. Prediction of aircraft specific energy along the intended trajectory appears to involve the prediction of airspeed, but using a constant nominal value of airspeed in Eq. (15) introduces a small, conservative error.

The first component of $\mathcal{F}$ in Eq. (15) is proportional to the rate of change of the horizontal wind component. If the wind field is assumed stationary, prediction of $\mathcal{F}$ along the intended trajectory could be made by differencing adjacent wind estimates:

$$\hat{\mathcal{F}}_j = 1/L\left(\hat{w}_{r_{jk}} - \hat{w}_{r_{j-1,k}}\right) \tag{16}$$

This would amplify high-frequency noise, resulting in excessive prediction error. Alternatively, predicted energy deviation and $\mathcal{F}$ can be computed by a Kalman filter algorithm using the wind estimates as inputs. $\mathcal{F}$ is obtained through a weighted sum of the radial wind estimates, with the weights selected by definition and minimization of a suitable cost function.

An important limitation of Doppler wind measurement devices is their inability to measure winds perpendicular to the direction of the Doppler pulse. As a consequence, the second component of $\mathcal{F}$ in Eq. (15), due to vertical winds, is not measured by the device. In downburst wind shears, head-tail wind shear is produced by vertically descending winds that flow outward as they near the ground. These downdraft winds pose a hazard to the aircraft that the Doppler sensors cannot directly measure. Current research is attempting to model the vertical wind as a function of the horizontal wind for hazard estimation.[23] In the simple downburst model of Ref. 23, the correlation between horizontal and vertical winds depends on the size of the downdraft, the altitude, and the distance from the downburst core. In a well-measured and well-studied microburst, four major downdraft regions were found.[24] As the relationship between horizontal and vertical winds remains to

be established, the present study is based on radial wind alone. If a consistent correlation between vertical wind and radial-wind measurement is found, vertical wind could be added to the stochastic model.

To predict the wind-shear-induced energy deviation E_{sw}, Eq. (14) can be integrated across a typical range gate j, resulting in the recursive form

$$E_{sw_j} = E_{sw_{j-1}} - \left(\frac{V_o L}{V_t}\right)\mathfrak{F}_{j-1_{av}} \tag{17}$$

where V_t is average inertial speed of the aircraft. $\mathfrak{F}_{av}$ is modeled as a stationary process driven by a discrete random sequence:

$$\mathfrak{F}_{j_{av}} = \mathfrak{F}_{j-1_{av}} + \eta_{j-1} \tag{18}$$

where η is a normally distributed white noise sequence with zero mean and standard deviation σ_η. This standard deviation is a design parameter that alters the response characteristics of the prediction filter, as demonstrated by simulation. Equations (17) and (18) may be written in vector-matrix form:

$$x_j = \begin{bmatrix} 1 & -\left(\frac{V_o L}{V_t}\right) \\ 0 & 1 \end{bmatrix} x_{j-1} + \begin{bmatrix} 0 \\ 1 \end{bmatrix} \eta_{j-1} \tag{19}$$

where

$$x_j = \left[E_{sw_j} \quad \mathfrak{F}_{j_{av}}\right]^T \tag{20}$$

The relationship between prediction and estimation is obtained by substitution of Eq. (15) into Eq. (14) and integration from the aircraft (denoted with subscript 0) to a typical range gate j. This results in the equation

$$w_{x_j} - w_{x_0} = -\left(\frac{g}{V_a}\right)(E_{sw_j} - E_{sw_0}) + \left(\frac{L}{V_t}\right) w_{h_{av}} \tag{21}$$

If the prediction is initialized with the condition

$$E_{sw_0} = -(V_a/g) w_{x_0} \tag{22}$$

then Eq. (21) may be rewritten as

$$w_{x_j} = \left[-\left(\frac{g}{V_o}\right) \quad 0\right] x_j + \left(\frac{gL}{V_o V_t}\right) w_{h_{av}} \tag{23}$$

In this paper vertical wind is modeled as a normally distributed white random sequence, uncorrelated with the radial winds, with mean and variance

$$E\{w_{h_j}\} = 0 \tag{24}$$

Table 1 Simulation parameters

Aircraft initial conditions	
Airspeed, V_o	160 Kt
Altitude, h	2000 ft
Inertial flight-path angle, γ_I	−3 deg
Distance to microburst core	20,100 ft
Doppler sensor	
Range gate separation, L	500 ft
Distance between sequences, d	27 ft
Noise standard deviation, σ_n	1 ft/s
Distance to aircraft	20,000 ft
Turbulence	
rms turbulence intensity, σ_u	2.7 ft/s
Turbulence scale length, L_u	1000 ft
Microburst	
Downdraft radius	2070 ft
Maximum horizontal winds	58.4 ft/s
Height of boundary layer	131 ft

and

$$E\{w_{h_j}^2\} = \sigma_{w_h}^2 \tag{25}$$

With the previously given model, prediction of the hazard level can be made from the output of the estimation Kalman filters after each measurement sequence. The wind estimates are processed using a recursive procedure based on the Kalman filter.[18,19] The prediction is initialized with onboard estimates of w_{x_0} and $\mathfrak{F}_0$. Predictions of E_{sw} and $\mathfrak{F}_{av}$, denoted $\hat{E}_{sw}$ and $\hat{\mathfrak{F}}$, are made for each range gate using the recursive equations

$$\hat{E}_{sw_j} = \hat{E}_{sw_{j-1}} - \frac{V_t}{gL}\hat{\mathfrak{F}}_{j-1} + K_{E_j}\left[\hat{w}_{r_{j1}} - \frac{g}{V_t}\hat{E}_{sw_{j-1}} - \frac{V_t}{gL}\hat{\mathfrak{F}}_{j-1}\right] \tag{26}$$

$$\hat{\mathfrak{F}}_j = \hat{\mathfrak{F}}_{j-1} + K_{\mathfrak{F}_j}\left[\hat{w}_{r_{j1}} - \frac{g}{V_t}\hat{E}_{sw_{j-1}} - \frac{V_t}{gL}\hat{\mathfrak{F}}_{j-1}\right] \tag{27}$$

These equations involve two gains, K_{E_j} and $K_{\mathfrak{F}_j}$, that are computed at each step based on the covariance propagation and filter gain computations of the Kalman filter.[18,19] The design parameter σ_η influences the size of these gains, influencing the response characteristics of the prediction filters.

Simulation of Stochastic Prediction Techniques

The stochastic estimation and prediction algorithms are demonstrated using a batch simulation of aircraft encounters with downburst wind shear and with severe turbulence. For each simulation, two different predictions are made, based on different choices of the design parameter σ_η. The wind shear is modeled by the Oseguera-Bowles stagnation-point-flow downburst model,[25] and severe turbulence is modeled using the Dryden spectrum as presented in Ref. 26. A twin-jet transport aircraft is represented by a point-mass longitudinal model,[27] trimmed along an approach path at a constant airspeed of 160 Kts. Normally distributed white noise is superimposed on measurements to simulate Doppler sensor error. Table 1 lists the parameters of the simulation.

The wind shear simulation is initiated with the microburst just out of the sensor's detection range. Figure 5 depicts the

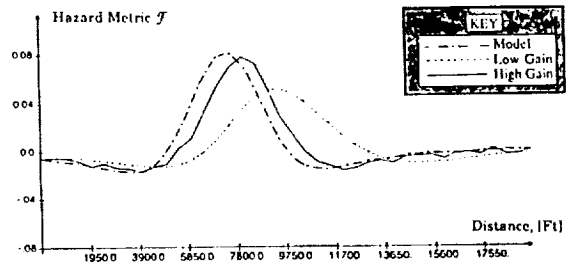

Fig. 5 Comparison of microburst model headwind-tailwind component of F-factor with predicted F-factor.

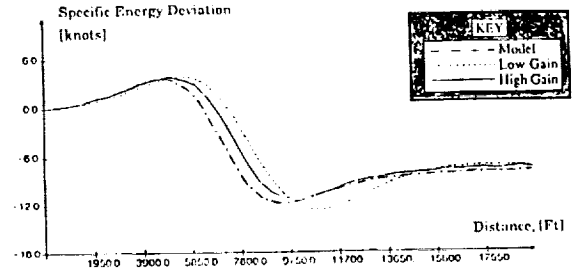

Fig. 6 Comparison of aircraft energy deviation due to headwind-tailwind shear and predicted energy deviation.

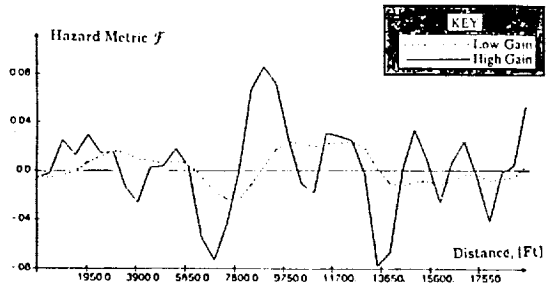

Fig. 7 Comparison of F-factor predictions in severe Dryden turbulence.

situation 10 s later, comparing the predicted hazard metric $\mathcal{F}_{a_v}$ along the flight path with the model's $\mathcal{F}_{a_v}$ component due to the headwind/tailwind shear alone. The predictions agree well with the model's head/tail wind component of $\mathcal{F}_{a_v}$, but the peak magnitude of the prediction is attenuated due to the finite bandwidth of the prediction algorithm. In addition, the distance between the aircraft and the wind shear is overpredicted due to phase shifting. With a lower value of σ_η, the estimators have lower gains, and these effects are more pronounced. If a wind shear warning were issued each time a critical value of $\mathcal{F}_{a_v}$ was exceeded, the algorithm with higher σ_η would have a greater chance of positively identifying severe wind shear.

For the same simulation, Fig. 6 compares the predicted energy deviation, normalized as an airspeed deviation, and the energy deviation due to the component of the wind shear. Although the error in prediction of distance to the microburst is greater for the lower value of σ_η, both predictions perform favorably in predicting peak energy loss. However, the total energy loss to the aircraft is greater than either prediction, due to the effect of the unobserved downdraft winds.

Figure 7 compares the predicted hazard metric $\mathcal{F}_{a_v}$ for each of the prediction designs in severe Dryden turbulence. The higher choice of σ_η results in greater response to turbulence. If wind shear warnings were issued each time a critical value of $\mathcal{F}_{a_v}$ was predicted, the algorithm with higher σ_η would issue more frequent false alarms. The optimization of a prediction algorithm must take into account both detection performance and false alarm prevention. Wavelengths corresponding to severe wind shear should be passed, but short wavelength disturbances that do not affect the flight path should be eliminated.

Conclusions

Doppler wind sensors can provide advance warning of a wind shear threat, but wind measurements are influenced by turbulence and measurement error. Optimal estimation provides a framework for minimizing the error of wind estimates given a hypothesis of the wind field structure. The estimation procedures presented here assume a structure to the local wind field at each range gate of the Doppler sensor, resulting in a bank of parallel Kalman filters. A first-order Markov turbulence model accounts for spatial correlation in the wind field due to turbulence. Measures of uncertainty are produced during the optimal estimation process. Stochastic prediction techniques are used to predict the impact of estimated winds on the energy performance of the aircraft. These techniques extend naturally to multiple Doppler sensors and could be expanded to predict other quantities such as altitude deviation error and touchdown dispersion error, given a nominal model of pilot compensation.

If wind shear warning is based on a critical threshold value of a hazard prediction, the detection reliability depends on the design of the prediction algorithm. Kalman-filter-based designs may be band limited, identifying areas with a sustained level of substantial wind shear. To further refine the algorithm, a comparative analysis of prediction algorithm designs can be conducted, using an ensemble of representative severe wind shear models. The potential for false warning in severe turbulence also can be compared. Both threshold and design bandwidth may be chosen to further optimize detection reliability.

Hazard prediction from Doppler sensors can provide the sole basis for a wind shear alert, but the lack of vertical wind estimates limits the alert's reliability. Other sources of information could improve the reliability of Doppler-based stochastic predictions through adaptive prediction techniques. Moreover, threshold exceedance of a hazard prediction could be viewed as uncertain evidence supporting a hypothesis of severe wind shear in the Bayesian network. With the reliability of threshold exceedance as evidence established through statistical analysis, hazard prediction can be incorporated into a probability-based expert system for wind shear avoidance.

Acknowledgment

This research has been sponsored by the NASA Langley Research Center under Grant NAG-1-834.

References

[1]Townsend, J., (ed.), *Low-Altitude Wind Shear and Its Hazard to Aviation*, National Academy Press, Washington, DC, 1983.

[2]*Windshear Training Aid*, U.S. Department of Transportation, Federal Aviation Administration, Associate Administrator for Development and Logistics, Washington, DC, Feb. 1987.

[3]Fujita, T. T., "The Downburst: Microburst and Macroburst," Satellite and Mesometeorology Research Project, University of Chicago, Chicago, IL, 1985.

[4]McCarthy, J., Roberts, R., and Schreiber, W., "JAWS Data Collection, Analysis Highlights, and Microburst Statistics," *Preprints, 21st Conference on Radar Meteorology*, American Meteorological Society, Boston, MA, 1983, pp. 596-601.

[5]Rinehart, R. E., and Isaminger, M. A., "Radar Characteristics of Microbursts in the Mid-South," *Preprints, 23rd Joint Conference on Radar Meteorology*, American Meteorological Society, Boston, MA, 1986, pp. J116-J119.

[6]Turnbull, D., McCarthy, J., Evans, J., and Zrnić, D., "The FAA Terminal Doppler Weather Radar (TDWR) Program," *Preprints, 3rd International Conference on the Aviation Weather System*, American Meteorological Society, Boston, MA, 1989, pp. 414-419.

[7]Barab, J. D., Page, R. D., Rosenburg, B. L., Zurinskas, T. E., and Smythe, G. R., "Evaluation of Enhancements to the Low Level Windshear Alert System (LLWAS) at Stapleton International Airport," Final Rept., DOT/FAA/PS-88/14, July 1987-March 1988.

[8]Campbell, S. D., and Olson, S., "Recognizing Low-Altitude Wind Shear Hazards from Doppler Weather Radar: An Artificial Intelligence Approach," *Journal of Atmospheric and Oceanic Technology*, Vol. 4, No. 1, March 1987, pp. 5-18.

[9]Campbell, S. D., "Microburst Precursor Recognition Using an Expert System Approach," *Preprints, Fourth International Conference on Interactive Information and Processing Systems for Meteorology, Oceanography, and Hydrology*, American Meteorological Society, Boston, MA, 1988.

[10]Roberts, R. D., and Wilson, J. D., "A Proposed Microburst Nowcasting Procedure Using Single-Doppler Radar," *Journal of Applied Meteorology*, Vol. 28, No. 4, April 1989, pp. 285-303.

[11]Saint, S., "The Missing Element in Wind Shear Protection," *Business Aircraft Meeting and Exposition*, Society of Automotive Engineers Rept. SAE 830715, April 1983.

[12]Zweifel, T., "Sensor Consideration in the Design of a Windshear Detection and Guidance System," *Aerospace Technology Conference and Exposition*, Society of Automotive Engineers Rept. SAE 881417, Oct. 1988.

[13]Bracalente, E. M., and Jones, W. R., "Airborne Doppler Radar Detection of Low Altitude Windshear," *Journal of Aircraft*, Vol. 27, No. 2, 1990, pp. 151-157.

[14]Targ, R., and Bowles, R. L., "Airborne LIDAR for Avoidance of Windshear Hazards," *Proceedings of the Second Combined Manufacturer's and Technology Airborne Windshear Review Meeting* (Williamsburg, VA), Vol. 1, Oct. 1988, pp. 369-377.

[15]Scott, W. B., "Researchers Develop Airborne Flir with Ability to Pinpoint Microbursts," *Aviation Week and Space Technology*, Feb. 17, 1990, pp. 69-71.

[16]Stengel, R. F., and Stratton, D. A., "An Expert System for Wind

Shear Avoidance," *Engineering Applications of Artificial Intelligence*, Vol. 2, No. 3, Sept. 1989, pp. 190-197.

[17]Stratton, D. A., and Stengel, R. F., "Probabilistic Reasoning for Intelligent Wind Shear Avoidance," *Proceedings of the 1990 AIAA Guidance, Navigation, and Control Conference*, AIAA, Washington, DC, 1990, pp. 1099-1107.

[18]Stengel, R. F., *Stochastic Optimal Control*, Wiley, New York, 1986.

[19]Anderson, B. D. O., and Moore, J. B., *Optimal Filtering*, Prentice-Hall, Englewood Cliffs, NJ, 1979.

[20]Bayes, T., "An Essay Towards Solving a Problem in the Doctrine of Chances," *Two Papers by Bayes*, Hafner, New York, 1963.

[21]Papoulis, A., *Probability, Random Variables, and Stochastic Processes*, McGraw-Hill, New York, 1984.

[22]Pearl, J., *Probabilistic Reasoning in Intelligent Systems: Networks of Plausible Inference*, Morgan Kaufmann, San Mateo, CA, 1988.

[23]Byrd, G. P., Proctor, F. H., and Bowles, R. L., "Evaluation of a Technique to Quantify Microburst Windshear Hazard Potential to Aircraft," *Proceedings of the 29th Conference on Decision and Control* (Honolulu, HI), Vol. 2, 1990, pp. 689-694.

[24]Proctor, F., "Model Comparison of July 7, 1990 Microburst," *Proceedings of the Third Combined Manufacturer's and Technology Airborne Windshear Review Meeting* (Williamsburg, VA), Vol. 1, 1990, pp. 81-103.

[25]Oseguera, R., and Bowles, R. L., "A Simple Analytic, 3-Dimensional Downburst Model Based on Boundary Layer Stagnation Flow," NASA TM-100632, July 1988.

[26]"Flying Qualities of Piloted Airplanes," Military Specification 8785-C, Wright-Patterson Air Force Base, OH, Nov. 1980.

[27]Hinton, D., "Flight Management Strategies for Escape from Microburst Encounters," NASA TM-4057, Aug. 1988.

Stochastic Measures of Performance Robustness in Aircraft Control Systems

SEE ALSO
93A 14595

Laura Ryan Ray*
Clemson University, Clemson, South Carolina 29634
and
Robert F. Stengel†
Princeton University, Princeton, New Jersey 08544

Stochastic robustness, a simple technique used to estimate the robustness of linear, time-invariant systems, is applied to a twin-jet transport aircraft control system. Concepts behind stochastic *stability* robustness are extended to stochastic *performance* robustness. Stochastic performance robustness measures based on classical design specifications and measures specific to aircraft handling qualities are introduced. Confidence intervals for comparing two control system designs are presented. The application of stochastic performance robustness, the use of confidence intervals, and tradeoffs between performance objectives are demonstrated by means of the twin-jet aircraft example.

Introduction

STANDARD linear control system design techniques rely on accurate models of the system to be controlled. Because models are never perfect, robustness analysis is necessary to determine the possibility of instability or inadequate performance in the face of uncertainty. Robustness to these uncertainties, parametric or unstructured, is normally treated deterministically and often without regard for possible physical variations in the system. Consequently, overconservative control system designs or designs that are insufficiently robust in the face of real-world uncertainties are a danger.

Stochastic robustness analysis (SRA), a simple technique to determine the robustness of linear, time-invariant systems by Monte Carlo methods, was introduced in Ref. 1 and presented in detail in Refs. 2 and 3. These references described stochastic stability robustness analysis and introduced the probability of instability as a scalar measure of stability robustness. Confidence intervals for the scalar probability of instability were presented, and the stochastic root locus, or probability density of the closed-loop eigenvalues, graphically portrayed robustness properties. Because it uses knowledge of the statistics of parameter variations directly, SRA provides an inherently precise yet simple characterization of robustness. The physical meaning behind the probability of instability is apparent, and overconservative or insufficiently robust designs can be avoided. Applications of SRA to full-state feedback aircraft control systems were described in Ref. 4. The results presented there illustrated the use of stochastic stability robustness techniques in comparing control system designs and in including finite-dimensional uncertain dynamics.

Concepts behind stochastic stability robustness can be extended to provide insight about control system design for performance. Design specifications such as rise time, overshoot, settling time, dead time, and steady-state error normally are used as indicators of adequate performance and lend themselves to the same kind of analysis as already described. Concepts of stochastic stability robustness analysis can be applied to these criteria giving probabilistic bounds on scalar performance criteria. Metrics resulting from SRA can be related to controller design parameters, thus providing a foundation for design tradeoffs and optimization. Extensions and uses of stochastic performance robustness in aircraft control system design and analysis are described in the following, and they are illustrated by means of an example.

Stochastic Performance Robustness

Stochastic stability robustness analysis is based on Monte Carlo analysis of the probability of instability P, and associated confidence intervals, given a statistical description of parameter uncertainty.[2-4] Because the stability test is binomial (i.e., the outcome of each Monte Carlo evaluation takes one of two values: stable or unstable), lower L and upper U confidence bounds are calculated using the binomial test.[5] While stability is an important element of robustness, performance robustness analysis is vital to determining whether important design specifications are met. Adequate performance, such as initial condition response, command response, control authority, and rejection of disturbances, is difficult to describe by a single scalar metric. Nevertheless, elements of stochastic stability robustness analysis apply for binomial performance metrics.

Numerous criteria stemming from classical control concepts exist as measures of adequate performance. Appealing to these, one can begin a smooth transition from stability robustness analysis to performance robustness analysis simply by analyzing the degree of stability or instability rather than strict stability. As described in Ref. 2, one method of doing this is to shift the vertical discriminant line from zero to $\Sigma <$ (or $>$) 0. Histograms and cumulative distributions for varying degrees of stability are readily given by the Monte Carlo estimate of the probability of any eigenvalue real-part exceeding Σ. Binomial confidence intervals are applicable to each point of the cumulative distribution as there are just two values of interest, e.g., satisfactory or unsatisfactory. P is a special case where $\Sigma = 0$. The robustness metric resulting from the cumulative probability distribution is directly related to classical concepts of rates of decay (growth) of first- and second-order closed-loop responses, time-to-half, and time-to-double. Taking degree-of-stability analysis further, rather than a vertical discriminant line, one can confine the closed-loop roots to sectors in the complex plane bounded by lines of constant damping and arcs of constant natural frequency.[6] Systems with roots

Presented as Paper 90-3410 at the AIAA Guidance, Navigation, and Control Conference, Portland, OR, Aug. 20-22, 1990; received Feb. 25, 1991; revision received Dec. 16, 1991; accepted for publication Jan. 2, 1992.

*Assistant Professor, Department of Mechanical Engineering. Member AIAA.

†Professor, Department of Mechanical and Aerospace Engineering. Associate Fellow AIAA.

Research supported by government grant.

confined to these regions would be expected to display a certain transient response speed. Again, the probability of roots lying within a sector follows a binomial distribution, and binomial confidence intervals apply.

Performance specifications for aircraft flying qualities are detailed in Ref. 7 in terms of longitudinal and lateral-directional criteria at three levels of performance for each flight phase. Many flying-qualities criteria require little computation above and beyond eigenvalue computation, making performance robustness as easy to characterize as stability robustness. For example, the short-period response can be characterized by its damping ratio and natural frequency vs normal acceleration sensitivity to angle-of-attack n_α. The latter is illustrated in Ref. 7 by plotting the short-period undamped natural frequency vs n_α, as shown in Fig. 1. n_α is simply a function of the dynamic pressure $\bar{q}$ and vehicle parameters

$$n_\alpha = \frac{\bar{q} S_{ref}}{mg} C_{L_\alpha} \tag{1}$$

C_{L_α} is the lift-curve slope, S_{ref} the wing reference area, m the mass, and g the gravitational constant. Short-period-mode requirement levels for each flight phase are characterized by calculating the closed-loop eigenvalues and evaluating Eq. 1. Repeated evaluations using Monte Carlo analysis give a distribution that can be shown pictorially on Fig. 1; the resulting measure of performance robustness is the probability of remaining within level 1, 2, or 3 criteria.[7] Binomial confidence interval computations can be applied to the scalar probability estimate.

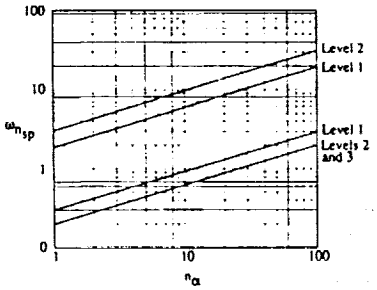

Fig. 1 Short-period response as characterized by n_α vs $\omega_{n_{sp}}$ for category B flight phase (climb, cruise, descent) and all aircraft classes.[7]

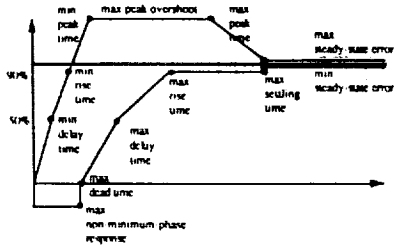

Fig. 2 Example of step response bounds formed by scalar performance characteristics.

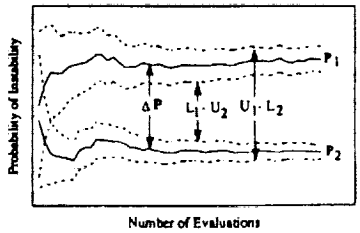

Fig. 3 Confidence interval calculation on the difference ΔP between two probabilities P_1 and P_2.

Table 1 Longitudinal parameters of the twin-jet aircraft

Uniform variation[a]	Description
15	Mass, slugs
15	Moment of inertia about the y axis, slug-ft^2
2	Wing reference area, ft
2	Aerodynamic chord, ft
2	Wing span, ft
30	Center-of-gravity location as a percent of mean aerodynamic chord
25	Lift-curve slope
25	Lift-curve intercept
40	Deviation of the basic lift coefficient due to Mach effects on lift-curve intercept
40	Deviation of the basic lift coefficient due to Mach effects on lift-curve slope
5	Variation in lift coefficient with rate of change of nondimensional α
7.5	Variation in lift coefficient with rate of change of nondimensional q
10	Variation in lift coefficient with change in elevator angle
50	Basic low-speed drag coefficient
25	Moment-curve slope
25	Moment-curve intercept
25	Deviation of the basic moment coefficient due to Mach effects on moment-curve intercept
10	Deviation in the basic moment coefficient due to Mach effects on moment-curve slope
10	Variation in moment coefficient with rate of change of nondimensional α
10	Variation in lift coefficient with rate of change of nondimensional q
15	Variation in moment coefficient with change in elevator angle
10	Center-of-gravity variation factor

[a] ± percent of nominal parameter value

Time responses provide the most clear-cut means of evaluating performance. Stochastic performance robustness can be portrayed as a distribution of possible trajectories around a nominal or desired trajectory. After defining "envelopes" around the nominal trajectory (Fig. 2), the probability of violating the envelopes can be computed using Monte Carlo evaluation. The envelope chosen around the nominal trajectory encompasses scalar performance measures; the trajectories in Fig. 2 are examples of bounds defined by minimum and/or maximum allowable dead time, delay time, rise time, time-to-peak overshoot, peak overshoot, settling time, and steady-state error.[6] Although it is simple to conclude that a response violates an envelope, individual responses within the envelope may not be acceptable. In such cases, the derivative of a response and envelopes around the derivative also can be used as performance criteria.[3]

The criteria defining envelopes that bound an acceptable time response are not unique; the segmented envelopes in Fig. 2 can be smoothed, or other scalars can be used to define points on the envelope. However, once an envelope is defined, time response distributions due to a command input, disturbance, initial condition, or some combination can be computed by Monte Carlo methods. For each evaluation, the trajectory is a binomial variable; it either stays within the envelope or violates the envelope, and binomial confidence intervals apply. Although individual time responses require more computation time than do individual sets of eigenvalues, such analysis is well within the capability of existing workstations.

Confidence intervals for the difference between two probabilities are useful when comparing two control system designs. A statistic on the difference decides whether one controller is more robust than another, either as part of an iterative design process or as imbedded in an optimization technique. The

Table 2 Scalar performance criteria defining command response envelope

Scalar metric	Value
Maximum dead time	2.5 s
Maximum nonminimum-phase response	−0.1 of desired steady-state value
Minimum and maximum delay time	1.0 s and 7.5 s
Minimum and maximum rise time	2.0 s and 15.0 s
Minimum and maximum peak time	3.0 s and 18.0 s
Maximum peak overshoot	1.25 of desired steady-state value
Maximum settling time	22.0 s
Minimum and maximum steady-state error	±0.025 of desired steady-state value

Table 3 Setpoint for individual velocity and flight-path-angle commands

Command	δT, %	δE, deg	V, fps	γ, deg	q, rad/s	α, deg
V = 15 fps	1.1	15.3	15	0	0	−0.25
γ = 4 deg	24.1	0.6	0	4	0	−0.01

statistics literature gives several methods of computing the confidence interval for the difference between two binomial variables. Reference 8 presents a method based solely on individual confidence intervals. Given individual intervals based on independent Monte Carlo trials,

$$\Pr(L_1 \le P_1 \le U_1) = 1 - \alpha_1 \tag{2}$$

$$\Pr(L_2 \le P_2 \le U_2) = 1 - \alpha_2 \tag{3}$$

the confidence interval around $\Delta P \triangleq P_1 - P_2$ is given by [8]

$$\Pr[(L_1 - U_2) \le \Delta P \le (U_1 - L_2)] \ge 1 - \alpha_1 - \alpha_2 + \alpha_1\alpha_2 \tag{4}$$

When identical parameter sets are used to generate individual intervals, the right-hand side of Eq. (4) is $1 - \alpha_1 - \alpha_2$. Since (L_1, U_1) and (L_2, U_2) are computed using the binomial test and represent exact intervals for the individual estimates, Eq. (4) is not an approximation. Confidence interval comparisons are illustrated schematically in Fig. 3. The interpretation of the confidence interval for the difference is straightforward; the probability that the true difference lies within $[(L_1 - U_2), (U_1 - L_2)]$ is at least $1 - \alpha_1 - \alpha_2 + \alpha_1\alpha_2$. If the interval on ΔP contains zero (i.e., if the individual intervals overlap as they do initially in Fig. 3), then the difference in robustness between the two systems is not proven significant at that number of evaluations. If the true difference ΔP is small, a larger number of evaluations may result in an interval that does not contain zero, as in Fig. 3.

A given ΔP can result from many combinations of individual probability estimates, and it is difficult to generalize the number of evaluations necessary to detect a difference of a certain magnitude. Nevertheless, the number of evaluations required for an individual confidence interval can be used to foretell the number of evaluations necessary to detect a difference between two estimates. Figure 4 gives the required number of evaluations J for each individual confidence interval, for the special case, $\alpha_1 = \alpha_2 = 0.05$. Using the difference $P_2 - P_1$ as the ordinate and P_1 as the abscissa, the curves show the minimum number of evaluations required to establish a significant difference. For example, if the probability estimates (denoted $\hat{P}$) are $\hat{P}_2 = 0.45$ and $\hat{P}_1 = 0.4$, Fig. 4 shows that a statistically significant difference (i.e., nonoverlapping confidence intervals) can be determined using approximately 1500 Monte Carlo evaluations. Individual estimates of $\hat{P}_2 = 0.15$ and $\hat{P}_1 = 0.1$ result in the same difference, but fewer than 750 evaluations are required to detect the difference. Figure 4 is based on individual confidence interval calculations, as presented in Ref. 3.

Performance Robustness of Longitudinal Controllers For a Jet Transport

SRA is applied to a twin-jet transport aircraft, with the goal of characterizing the performance robustness of longitudinal

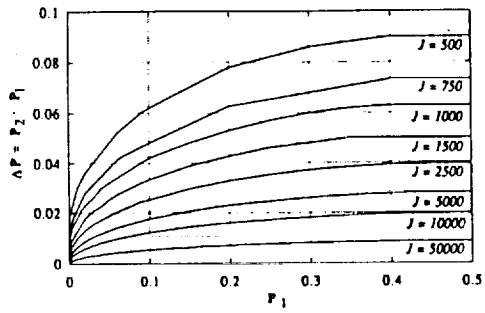

Fig. 4 Number of evaluations establishing significant differences between two probabilities for 95% confidence intervals and equal numbers of evaluations for individual probabilities.

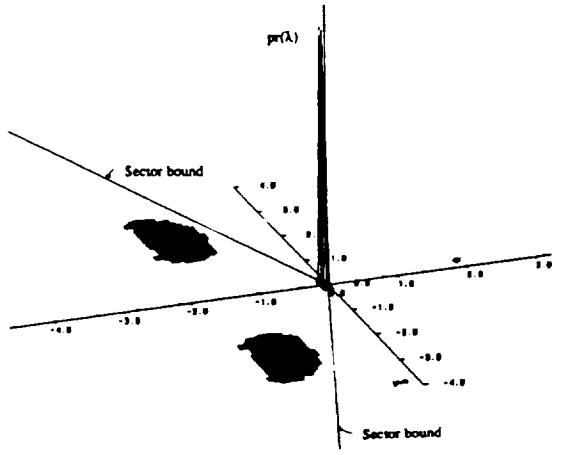

a) Stochastic root locus with sector bounds defined by minimum level 1 short-period damping for cruise flight

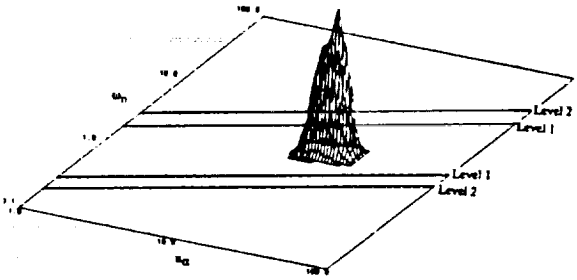

b) Short-period frequency vs acceleration sensitivity distribution

Fig. 5 Stochastic robustness evaluation of the open-loop short-period dynamics of the twin-jet aircraft, based on 10,000 Monte Carlo evaluations.

command responses. The rigid-body nonlinear longitudinal equations are

$$\begin{bmatrix} \dot{V} \\ \dot{\gamma} \\ \dot{q} \\ \dot{\alpha} \end{bmatrix} = \begin{bmatrix} \dfrac{-D + T\cos(\alpha)}{m} - g\sin(\gamma) \\ \dfrac{L + T\cos(\alpha)}{mV} - \dfrac{g\cos(\gamma)}{V} \\ \dfrac{M}{I_{yy}} \\ q - \dot{\gamma} \end{bmatrix} \tag{5}$$

where $[V, \gamma, q, \alpha]$ represent velocity, flight-path-angle, pitch rate, and angle-of-attack, $[L, D, M]$ are aerodynamic lift, drag, and pitching moment, T is the thrust, and g is the gravitational constant. Equation (5) depends on a number of parameters given in Table 1. Mean parameter values of the stability derivatives in Table 1 are functions of Mach number and altitude; they are interpolated from aerodynamic data curves for the aircraft at a given trim condition.[9] The aerodynamic model used to compute L, D, and M is a simplified version of that given in Ref. 9, modified to use only two longitudinal controls (thrust and elevator). In this example, each Monte Carlo evaluation begins with the nonlinear equations of motion and associated parameters. The nonlinear equations are evaluated using appropriately distributed random parameters and are then linearized around the nominal trim condition. The closed-loop eigenvalues and performance metrics are evaluated from the linearized system.

The parameters are assumed to have uniform variations of the magnitudes given in Table 1. For the wing parameters (S_{ref}, chord, span), these variations are representative of loose manufacturing tolerances. The mass and moment-of-inertia variations are based on the maximum and minimum possible values of these parameters given in Ref. 9. The remaining parameter-variation estimates are based on interpolation accuracy and possible flight condition variations around the nominal value.

Trim conditions for a flight condition of $V = 425$ fps (130 m/s) at an altitude of 5000 ft (1524 m) are as follows: thrust = 27.3%, elevator = −0.65 deg, and angle-of-attack = 2.15 deg. The open-loop eigenvalues for the state matrix resulting from linearizing Eq. (5) around trim are $\lambda = -1.32 \pm 2.44j$, $-0.0053 \pm 0.0962j$. Stochastic robustness evaluation using the short-period Mil-spec requirements[7] shows an acceptable open-loop short-period mode for the uniform parameter variations given in Table 1. Figure 5a shows the stochastic root locus with sectors defined by minimum level 1 short-period damping ratio for cruise or climb (category B flight phase); for 10,000 evaluations, the short-period eigenvalues never violate the level 1 damping restriction. Figure 5b characterizes the short-period frequency vs acceleration sensitivity, which also remains within level 1 constraints for 10,000 evaluations. The probability estimate of violating level 1 short-period specifications is 0, with 95% confidence intervals of (0, 3.69E − 4).

Design of Longitudinal Controllers

A command response that stays within the envelope described by scalar criteria in Table 2 serves as the performance requirement for designing linear regulators for velocity and flight-path-angle commands. In addition, elevator deflections are limited to ±30 deg, and thrust commands must remain between 0 and 100%. The desired commands $y^* = V^*$ or $y^* = \gamma^*$ and corresponding setpoints $\mathbf{x}^* = [V\ \gamma\ q\ \alpha]^T$, $\mathbf{u}^* = [\delta T\ \delta E]$ are given in Table 3. The open-loop responses to individual velocity and flight-path-angle commands are inadequate because of the slow, lightly damped phugoid mode. Numerical values of the results that follow depend heavily on the performance criteria chosen. The envelopes defined in Table 2 reflect tolerable variations around an acceptable nominal response. The control limits are typical of those for a jet transport. Changing the time response envelopes or control authority limits would give different numerical results. The emphasis in this example is not on the specific criteria chosen, but on how SRA characterizes performance given a control system design and performance specifications.

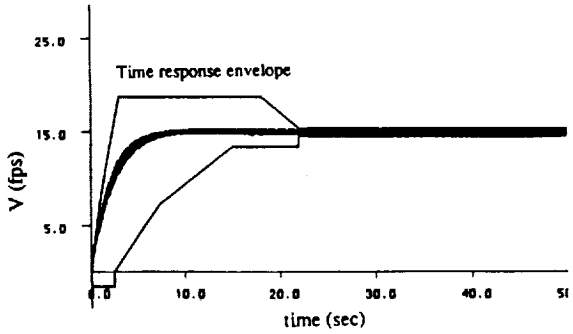

a) 15 fps velocity command: velocity response

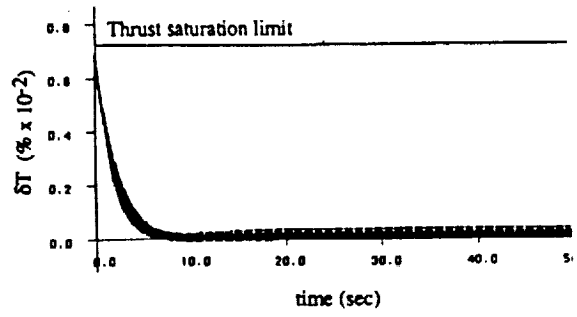

b) 15 fps velocity command: thrust response

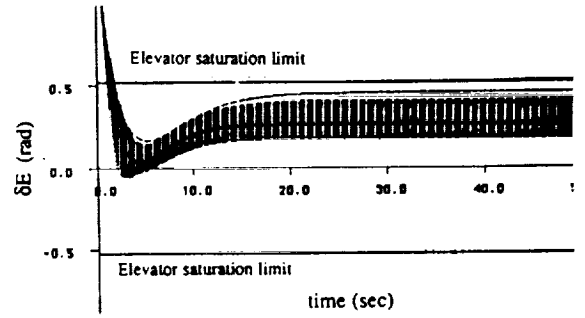

c) 15 fps velocity command: elevator response

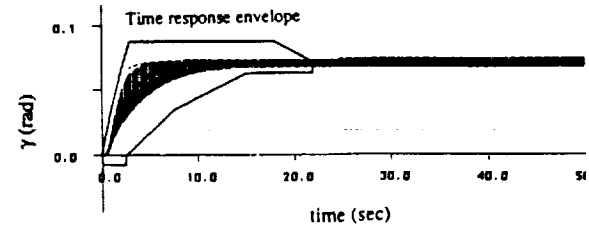

d) 4-deg flight-path-angle command: flight-path-angle response

Fig. 6 Closed-loop command responses using IMF controller, 500 Monte Carlo evaluations. Nominal response is indicated by the solid line.

Structured linear-quadratic regulators[10] offer a simple means of designing a linear control system with desirable performance and robustness characteristics. Specifications of the linear-quadratic performance index and subsequent control gains using implicit-model-following (IMF) minimizes the dynamic response error between the closed-loop system and an ideal model.[10] State, control, and cross-weighting matrices (Q, R, M) are based on a quadratic cost function that weights the difference between the actual state rate ($\dot{x}$) and that of an ideal model ($\dot{x}_M$), where

$$\dot{x}_M = F_M x_M \tag{6}$$

IMF offers a straightforward way of designing controllers that approximate desired dynamic characteristics. For this example, the ideal model was chosen to increase the natural frequency and damping of the phugoid mode, while maintaining acceptable short period response:

$$F_M = \begin{bmatrix} -0.3 & -32.17 & -0.0104 & -23.34 \\ 0.00381 & -0.1949 & 0.0006 & 1.356 \\ 0.0 & -0.0 & -1.273 & -5.981 \\ -0.0038 & 0.1949 & 0.999 & -1.356 \end{bmatrix} \tag{7}$$

$$\gamma_M = \begin{cases} -1.35 \pm 2.39j \\ -0.213 \pm 0.314j \end{cases} \tag{8}$$

Stochastic performance robustness analysis is based on the probability of violating the desired time response envelopes ($\hat{P}_V$ and $\hat{P}_\gamma$) and the probability of control saturation ($\hat{P}_{\delta T}$ and $\hat{P}_{\delta E}$).

The IMF controller gives a nominal closed-loop command response to separate velocity (Figs. 6a–c) and flight-path-angle (Fig. 6d) commands that is within the acceptable time-response envelope. Figure 6 also shows 500 Monte Carlo evaluations of the command response; the nominal steady-state control inputs and state are given in Table 3, and the nominal response in Fig. 6 is indicated by a solid line. The response and associated envelopes in Fig. 6 are shown for the commanded variable only; the remaining state elements do not require performance constraints in this example. Thrust and elevator time histories are shown for the velocity command response only. Parameter uncertainty effects appear as variations around the nominal response, indicated by the dark distribution and associated outliers. Parameter uncertainty results in a distribution of transient responses that stays within the envelope, and nonzero steady-state errors that violate the envelope for both velocity (Fig. 6a) and flight-path-angle (Fig. 6d) commands. Based on 500 Monte Carlo time response evaluations, the estimate $\hat{P}_V$ is 0.002 with 95% confidence intervals (5.1E − 5, 0.0111) and the estimate $\hat{P}_\gamma$ is 0.368 (0.326, 0.412). The nominal elevator response violates control limits for both command responses, and in each case, the probability of elevator saturation is $\hat{P}_{\delta E} = 1.0$. Note that the control saturation limits in Figs. 6b–c are adjusted to reflect the remaining control authority after considering trim requirements.

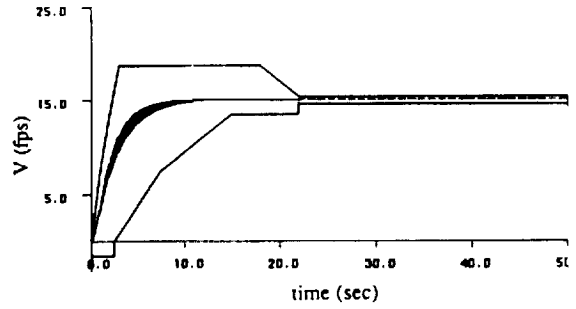

a) 15 fps velocity command: velocity response

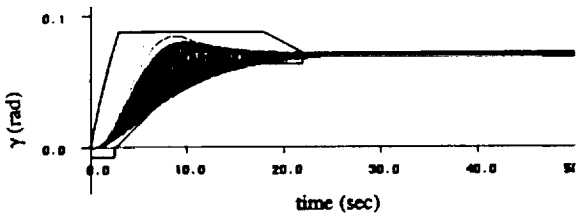

d) 4-deg flight-path-angle command: flight-path-angle response

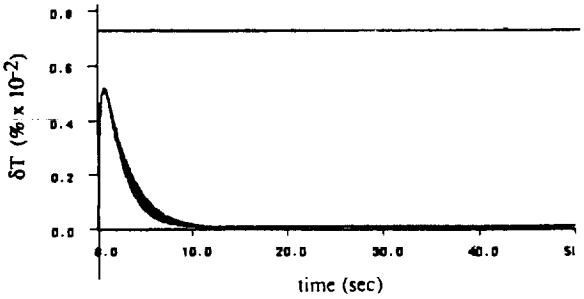

b) 15 fps velocity command: thrust response

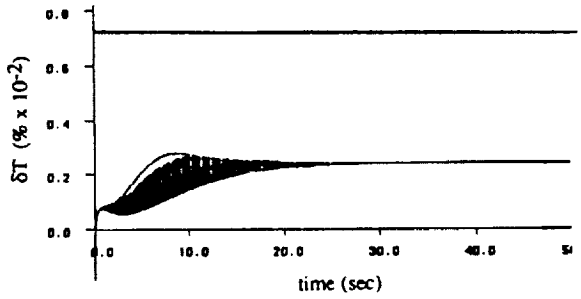

e) 4-deg flight-path-angle command: thrust response

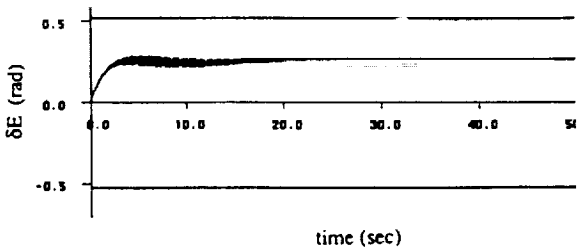

c) 15 fps velocity command: elevator response

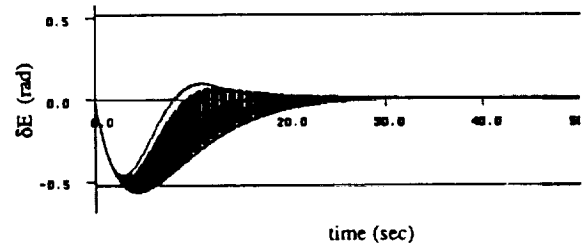

f) 4-deg flight-path-angle command: elevator response

Fig. 7 Closed-loop command response using PFIMF controller, with filter control weighting R_f = diag(10, 50), 500 Monte Carlo evaluations. Nominal response is indicated by the solid line.

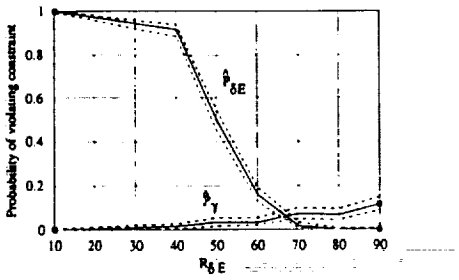

Fig. 8 Stochastic performance robustness evaluation with PFIMF: Probability of violating flight-path-angle command response $\hat{P}_{\gamma}$ and probability of violating elevator saturation limits $\hat{P}_{\delta E}$ vs filter weight $R_{\delta E}$. Solid lines give probability estimates, dashed lines give confidence intervals.

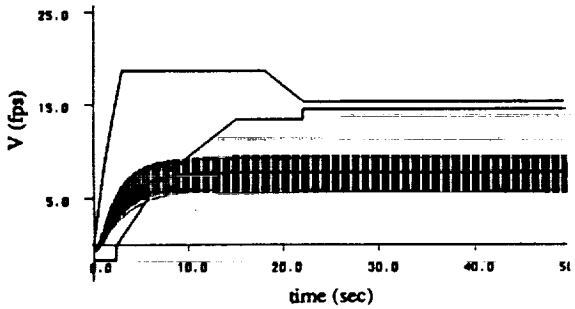

Fig. 9 Closed-loop command response using PFIMF controller, with filter control weighting $\mathbf{R}_F$ = diag(10, 50), 500 Monte Carlo evaluations: 15 fps velocity command subject to constant disturbance w_v = 40 fps. Nominal response is indicated by the solid line.

Implicit model following modified by state augmentation[10] can help meet control authority constraints. Proportional-filter (PF) compensation adds integrators to restrict the control rates, thus preventing instantaneous control changes and reducing the maximum control effort. The control vector is appended to the state vector

$$\begin{bmatrix} \dot{\bar{\mathbf{x}}} \\ \dot{\bar{\mathbf{u}}} \end{bmatrix} = \begin{bmatrix} \mathbf{F} & \mathbf{G} \\ \mathbf{0} & \mathbf{0} \end{bmatrix} \begin{bmatrix} \bar{\mathbf{x}} \\ \bar{\mathbf{u}} \end{bmatrix} + \begin{bmatrix} \mathbf{0} \\ \mathbf{I} \end{bmatrix} v(t) \tag{9}$$

where $\mathbf{F}$ and $\mathbf{G}$ are the nominal dynamic and control effect matrices, $\bar{\mathbf{x}} = \mathbf{x}(t) - \mathbf{x}^*$, $\bar{\mathbf{u}} = \mathbf{u}(t) - \mathbf{u}^*$, and $v(t)$ is a commanded control rate. The PFIMF state weighting matrix is

$$\mathbf{Q}_F = \begin{bmatrix} \mathbf{Q} & \mathbf{M} \\ \mathbf{M}^T & \mathbf{R} \end{bmatrix} \tag{10}$$

where $\mathbf{Q}$, $\mathbf{R}$, $\mathbf{M}$ are the original (IMF) weighting matrices. A weighting matrix, $\mathbf{R}_F$, constrains the control rates. Elements of $\mathbf{R}_F$ affect the bandwidth of each control; the larger the weight, the more the control rate is restricted.

The IMF regulator is augmented to include low-pass filtering of the control command, with a diagonal control-rate weighting matrix $\mathbf{R}_F$ = diag[10, 50]. Figure 7 shows 500 stochastic state and control histories to individual velocity and flight-path-angle commands using the PFIMF controller and a stream of random numbers independent from the IMF case. The (1, 1) element of $\mathbf{R}_F$ ($R_{\delta T}$) determines the amount of filtering on thrust rate, and the (2, 2) element ($R_{\delta E}$) controls elevator rate. With filter elements, the control rates are no longer unlimited, and the mean control responses remain unsaturated. Steady-state error due to parameter uncertainty remains within the desired state history envelope for the velocity command response (Fig. 7a). Steady-state error for the γ command improves, although the variation in the γ transient response is much greater than that of the IMF regulator alone, as seen by comparing Figs. 6d and 7d. $\hat{P}_V$ and $\hat{P}_{\gamma}$ estimates corresponding to Fig. 7 are 0.0 (0.0, 0.0074) and 0.034 (0.0199, 0.0539), respectively. For 500 evaluations, the PFIMF flight-path-angle command response improvement over the IMF case alone proves significant by application of confidence intervals on the difference ($P_{\gamma \text{IMF}} - P_{\gamma \text{PFIMF}}$). Applying Eq. 4,

$$\Pr[0.2721 \le (P_{\gamma \text{IMF}} - P_{\gamma \text{PFIMF}}) \le 0.3921] \ge 0.9025 \tag{11}$$

Equation 11 states that with PF augmentation between 27 and 39%, more of the flight-path-angle responses lie within the envelope, with a confidence coefficient of at least 0.9025. The mean elevator response for the flight-path-angle command dips just to saturation limits, and the probability of elevator saturation is $\hat{P}_{\delta E_{\text{PFIMF}}} = 0.502$ (0.457, 0.547).

Stochastic robustness analysis shows that PF augmentation improves performance objectives by reducing control rates and steady-state error due to uncertainty. The state and control response to the velocity command prove acceptable ($\hat{P}_V$, $\hat{P}_{\delta E}$, and $\hat{P}_{\delta T}$ all equal 0), and the improved responses to flight-path-angle command are statistically significant. For the flight-path-angle command, SRA demonstrates the tradeoff between the two performance objectives; increasing the (2, 2) element ($R_{\delta E}$) of $\mathbf{R}_F$ will further reduce elevator command authority at the expense of the γ time response. Figure 8 illustrates this tradeoff by showing $\hat{P}_{\gamma}$, $\hat{P}_{\delta E}$, and their confi-

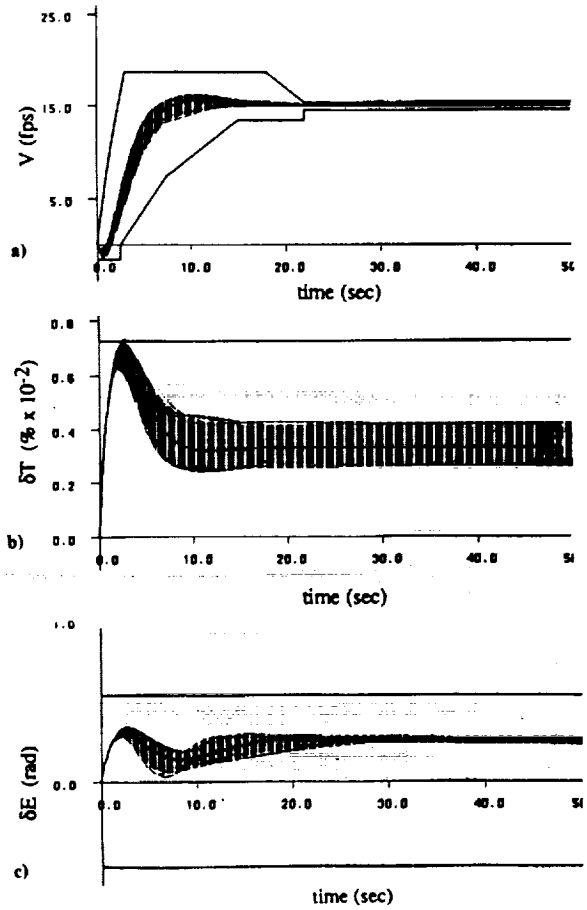

Fig. 10 Closed-loop command response using PIFIMF controller, with filter control weighting $\mathbf{R}_F$ = diag(200, 50), and integral state weighting $\mathbf{Q}_I$ = diag(0.1, 100), 500 Monte Carlo evaluations: 15 fps velocity command subject to constant disturbance w_v = 40 fps. Nominal response is indicated by the solid line.

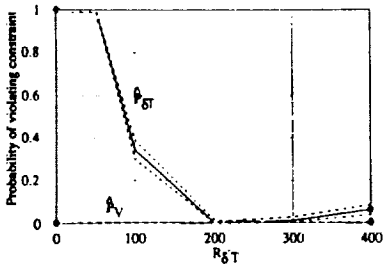

Fig. 11 Stochastic performance robustness evaluation with PIFIMF: Probability of violating velocity command response envelope $\hat{P}_V$ and probability of violating thrust saturation limits $\hat{P}_{\delta T}$ vs filter weight $R_{\delta T}$. Solid lines give probability estimates, dashed lines give confidence intervals.

dence intervals as functions of the design parameter $R_{\delta E}$. A plot like Fig. 8 can be used to choose the filter weight that gives the smallest probabilities of envelope violation while adhering as well as possible to the control authority restrictions. In this case, it is not possible to simultaneously reduce $\hat{P}_\gamma$ and $\hat{P}_{\delta E}$ to zero by varying $R_{\delta E}$. Nevertheless, stochastic robustness analysis offers a simple, understandable means of relating design parameters to performance objectives and of choosing the best control gains to meet those objectives.

Design of a Longitudinal Controller for Disturbance Rejection

As a final example, the preceding analysis is extended to encompass a performance constraint on disturbance rejection. The equations of motion are modified to include a vertical wind disturbance w_v

$$\begin{bmatrix} \dot{V} \\ \dot{\gamma} \end{bmatrix} = \begin{bmatrix} \dfrac{-D\sin(\alpha-\alpha_a)+T\cos(\alpha-\alpha_a)}{m} - g\sin(\gamma) \\ \dfrac{L\sin(\alpha-\alpha_a)+T\cos(\alpha-\alpha_a)}{mV} - \dfrac{g\cos(\gamma)}{V} \end{bmatrix} \tag{12}$$

where

$$\alpha_a = \alpha + \gamma - \tan^{-1}\frac{V\sin(\gamma)+w_v}{V\cos(\gamma)} \tag{13}$$

With the disturbance present, the state components represent inertial velocity, flight-path-angle, pitch, and angle-of-attack, and the disturbance enters through the expression for air-relative angle-of-attack α_a. A disturbance input matrix is defined for robustness analysis by numerical linearization of the nonlinear equations with respect to w_v, around the nominal condition $w_v = 0$. Velocity command response subject to a constant 40-fps vertical velocity disturbance using the PFIMF controller is shown in Fig. 9. The mean response shows a nonzero steady-state error that violates the command response envelope, and uncertainty causes a larger spread around the nominal response than that of the system without the disturbance (Fig. 7). Also, the steady-state flight-path-angle (not shown) is less than zero due to the disturbance.

Proportional-integral (PI) compensation introduces a command-error integral for each commanded state element, zeroing steady-state error and improving disturbance rejection characteristics. The perturbation equations for the nominal system are

$$\begin{bmatrix} \dot{\bar{x}} \\ \dot{\xi} \end{bmatrix} = \begin{bmatrix} \mathbf{F} & \mathbf{0} \\ \mathbf{H} & \mathbf{0} \end{bmatrix} \begin{bmatrix} \bar{x}(t) \\ \xi(t) \end{bmatrix} + \begin{bmatrix} \mathbf{G} \\ \mathbf{0} \end{bmatrix} \bar{u}(t) \tag{14}$$

$$\mathbf{H} = \begin{bmatrix} 1 & 0 & 0 & 0 \\ 0 & 1 & 0 & 0 \end{bmatrix} \tag{15}$$

where

$$\xi(t) = \xi(0) + \int_0^t \bar{y}(\tau)\,d\tau \tag{16}$$

and $\bar{y}(t) = y(t) - y^*$. Here, $y^* = [V\ \gamma]^T$, and a (2×2) weighting matrix $\mathbf{Q}_I$ is appended to the original state weighting matrix. Diagonal elements of $\mathbf{Q}_I$ affect the rate at which the command error integrals approach zero. The diagonal components are chosen to keep the velocity command within the desired envelope and to zero the flight-path-angle response. Command error integrals are added to the existing PFIMF controller, and for the resulting PIFIMF system with $\mathbf{Q}_I = \text{diag}[0.01, 100]$ and $\mathbf{R}_F = \text{diag}[200, 50]$, Fig. 10 shows an improved velocity command response $y^* = [V^*\ 0]^T$. The 500-evaluation probability estimates and 95% confidence intervals are $\hat{P}_V = 0$ (0.0, 7.4E-3) and $\hat{P}_{\delta T} = 0.002$ (5.1E-5, 0.0111). The (1, 1) component of $\mathbf{R}_F$ is increased to restrain thrust as the command error integrals are introduced. Figure 11 shows analysis of the tradeoff between $\hat{P}_V$ and $\hat{P}_{\delta T}$ as a function of design parameter $R_{\delta T}$ comparable to that presented for the flight-path-angle response in Fig. 8. Again, Fig. 11 can be used to choose control system design parameters that best meet performance objectives.

Conclusion

Stochastic robustness analysis offers a rigorous yet straightforward alternative to other robustness metrics that is simple to compute and is unfettered by normally difficult problem statements, such as non-Gaussian statistics, products of parameter variations, and structured uncertainty. The analysis embraces both stability and performance metrics, handling qualities requirements, and more general responses. Binomial confidence intervals provide statistical bounds on the probability of instability and on performance metrics. Statistical comparisons of control system robustness also are rendered through confidence intervals. Both stability and performance metrics resulting from stochastic robustness analysis provide details relating system specifications intrinsic to a given application and control system design parameters. Stochastic robustness analysis has a significant role to play in computer-aided control system design.

Acknowledgments

This research has been sponsored by the Federal Aviation Administration and the NASA Langley Research Center under Grant No. NGL 31-001-252 and by the Army Research Office under Grant No. DAAL03-89-K-0092.

References

[1]Stengel, R. F., "Some Effects of Parameter Variations on the Lateral-Directional Stability of Aircraft," *Journal of Guidance and Control*, Vol. 3, No. 2, 1980, pp. 124-131.

[2]Stengel, R. F., and Ray, L. R., "Stochastic Robustness of Linear Time-Invariant Control Systems," *IEEE Transactions on Automatic Control*, Vol. 36, No. 1, 1991, pp. 82-87.

[3]Ray, L. R., *Stochastic Robustness of Linear Multivariable Control Systems: Towards Comprehensive Robustness Analysis*, Ph.D. Dissertation, Dept. of Mechanical and Aerospace Engineering, Princeton Univ., MAE-1902-T, Princeton, NJ, 1991.

[4]Ray, L. R., and Stengel, R. F., "Application of Stochastic Robustness to Aircraft Control Systems," *Journal of Guidance, Control, and Dynamics*, Vol. 14, No. 6, 1991, pp. 1251-1259.

[5]Conover, W. J., *Practical Non-Parametric Statistics*, Wiley, New York, 1980.

[6]Franklin, G. F., et al., *Feedback Control of Dynamic Systems*, Addison-Wesley, Reading, MA, 1991.

[7]*Military Specification Flying Qualities of Piloted Airplanes*, U.S. Air Force, MIL-F-8785C, Wright-Patterson AFB, OH, Nov. 1980.

[8]Lavenberg, S. S., (ed.), *Computer Performance Modeling Handbook*, Academic, New York, 1983.

[9]*TVC Simulation Engineering Manual*, Boeing Co., Jan. 1982.

[10]Stengel, R. F., *Stochastic Optimal Control: Theory and Application*, Wiley, New York, 1986, Chap. 6.

REPORT DOCUMENTATION PAGE

Form Approved
OMB No. 0704-0188

1. AGENCY USE ONLY *(Leave blank)*	2. REPORT DATE	3. REPORT TYPE AND DATES COVERED
	February 1994	Conference Publication

4. TITLE AND SUBTITLE
FAA/NASA Joint University Program for Air Transportation Research 1992–1993

5. FUNDING NUMBERS
505-64-52-01

6. AUTHOR(S)
Frederick R. Morrell, Compiler

7. PERFORMING ORGANIZATION NAME(S) AND ADDRESS(ES)
NASA Langley Research Center
Hampton, VA 23681-0001

8. PERFORMING ORGANIZATION REPORT NUMBER
L-17366

9. SPONSORING/MONITORING AGENCY NAME(S) AND ADDRESS(ES)
Federal Aviation Administration
Washington, DC 20546 and
National Aeronautics and Space Administration
Washington, DC 20546-0001

10. SPONSORING/MONITORING AGENCY REPORT NUMBER
NASA CP-3246
DOT/FAA/CT-94/03

11. SUPPLEMENTARY NOTES

12a. DISTRIBUTION/AVAILABILITY STATEMENT
Unclassified–Unlimited

Subject Category-01

12b. DISTRIBUTION CODE

13. ABSTRACT *(Maximum 200 words)*

This report summarizes the research conducted during the academic year 1992–1993 under the FAA/NASA sponsored Joint University Program for Air Transportation Research. The year end review was held at Ohio University, Athens, Ohio, June 17–18, 1993. The Joint University Program is a coordinated set of three grants sponsored by the Federal Aviation Adminstration and NASA Langley Research Center, one each with the Massachusetts Institute of Technology (NGL-22-009-640), Ohio University (NGR-36-009-017), and Princeton University (NGL-31-001-252). Completed works, status reports, and annotated bibliographies are presented for research topics, which include navigation, guidance, and control theory and practice, aircraft performance, human factors and air traffic management. An overview of the year's activities for each university is also presented.

14. SUBJECT TERMS
Aircraft guidance; Avionics; Navigation and control; Human factors; Air traffic management

15. NUMBER OF PAGES
173

16. PRICE CODE
A08

17. SECURITY CLASSIFICATION OF REPORT	18. SECURITY CLASSIFICATION OF THIS PAGE	19. SECURITY CLASSIFICATION OF ABSTRACT	20. LIMITATION OF ABSTRACT
Unclassified	Unclassified	Unclassified	